Harnessing Drones, Doves and Sentinel-2 Imagery for Assessing the Composition and Trajectory of Restoration

Lewis Trotter *, Adam T Cross, Erin Rice, Todd P Robinson

Posted Date: 7 December 2023

doi: 10.20944/preprints202312.0441.v1

Keywords: drone monitoring; rehabilitation; multispectral imagery; fractional cover mapping; PlanetScope

Article

Harnessing Drones, Doves and Sentinel-2 Imagery for Assessing the Composition and Trajectory of Restoration

Lewis Trotter [1]*, Adam Cross [2], Erin Rice [3] and Todd Robinson [1]

[1] School of Earth and Planetary Sciences, Curtin University, Perth, WA 6845, Australia (lewis.trotter@postgrad.curtin.edu.au; T.Robinson@curtin.edu.au)
[2] School of Molecular and Life Sciences, Curtin University, Perth, WA 6845, Australia (Adam.Cross@curtin.edu.au)
[3] Water Corporation, 273 Bannister Rd, Canning Vale, WA 6155, Australia (Erin.Rice@watercorporation.com.au)
* Correspondence: lewis.trotter@postgrad.curtin.edu.au

Abstract: Natural vegetation restoration can take decades to achieve and requires information on species composition and trend to inform management strategies. Here we demonstrate the potential and portability of drone, dove and Sentinel-2 imagery for species level classification and trajectory monitoring using three study sites with different revegetation histories. Drone imagery (4 cm) was classified using random forests. Dove (3 m) and Sentinel-2 (10 m) images were acquired close to the anniversary of the drone flights and converted into fractional cover maps showing the proportion of exotics, natives and other land covers using ordinary least squares (OLS) and geographically weighted regression (GWR). The time series of fractional cover maps were converted into positive and negative slope and second-order curvature and summarised as one RGB composite to illustrate trend and observe exotic expansion. Drone classification accuracies ranged from 73%-76% when applied to the full plant species list and between 93% and 97% when grouped into natives, exotics, and other land covers. GWR outperformed OLS for all fractional cover mapping and GWR with dove imagery was more accurate than with Sentinel imagery. The combination of very high-resolution drone acquired imagery with the versatility of dove acquired imagery arms land managers with highly accurate species composition and their spatio-temporal dynamics to promote timely intervention.

Keywords: drone monitoring; rehabilitation; multispectral imagery; fractional cover mapping; PlanetScope

1. Introduction

Natural vegetation restoration following intentional clearing is broadly seen as successful if the previous plant community composition is replaced and biomass is tracking towards a benchmark [1]. This simplistic view does not consider the decades it can take for a site to regain most of its biodiversity and ecosystem attributes [2,3] nor the myriad of factors that can derail it such as weed invasions or changes to the fire regime. Indeed, the path to restoration is a dynamic one, requiring both short- and long-term monitoring. Short-term monitoring needs to allow for the potential to intervene, such as by removal of weeds, to accomplish long term success. Longer term monitoring should explore change and trajectory to evaluate success and/or refine strategies that will lead to success [4].

UAV's (or "drones") have been hailed as the key to revolutionising spatial ecology for over a decade [5], though this is deemphasised by some who suggest that processing workflows are still nascent in this space [6,7]. Nevertheless, imagery acquired from drones offers the greatest spatial resolution available today and is usually more cost-effective when areas of interest are much smaller (e.g., 10 ha) than the scene sizes of very high-resolution satellite imagery [8]. Drone captures are useful for informing the short-term monitoring needs of species composition [9]. However, repeat acquisitions require that ground crews be available to remotely pilot the UAV on anniversary dates, which can be more challenging.

 doi:10.20944/preprints202312.0441.v1

Sun synchronous satellites like Sentinel-2 are constantly collecting imagery, which minimises the logistical overhead of UAV flights [10] and guarantees an image will always be available around anniversary dates. However, the spatial resolution of most research focussed satellites (c. 10 m) limits the detection of individual plants. Planet's Dove and Superdove satellites consist of multiple large flocks of cubesats, which collect images of the Earth daily at 3-5 m resolution. This makes them one of, if not, the greatest source of data for fine scale real-time monitoring available today. Cubesats are tiny satellites when compared to Sentinel-2 or Landsat weighing around 4 kg and orbiting at around 400 km. Imagery is provided in RGB and near infrared at small cost [11].

A practical monitoring system that combines the advantages of the very high resolution of UAV imagery and the seamless acquisition of satellite imagery has potential to feed both the short- and long-term requirements of rehabilitation assessments. Fractional cover mapping can utilise the very high-resolution discrete classifications from drone imagery to derive fractions of land covers within pixels of lower resolution (e.g. Sentinel or Planet imagery). For example, a plant occupying a third of a 10 m pixel would be classified as 33% coverage. Repeat fractional cover mapping provides the necessary consistent assessment of vegetation coverage through time to make ecological management decisions, particularly around the trajectory of rehabilitation [12].

The Water Corporation of Western Australia are permitted to clear native vegetation in the process of their operations (e.g., water supply, wastewater, irrigation, drainage). Cleared vegetation requires restoration to meet regulatory requirements. Monitoring is for at least 2 years, but there is an expectation to monitor for longer in the future before relinquishment. Ground based surveys are not persistent enough to be relied on for management response through intervention. An operational remote sensing approach would assist monitoring of native and exotic vegetation distribution and change over time. Here, we explore three study sites of differing species composition and rehabilitation age for the potential to integrate both UAV and satellite imagery to aid in on-going monitoring of vegetation restoration. We have the following aims: (1) determine useful image-derived variables for discriminating between native and exotic species; (2) compare classification performance of native and exotic species; and (3) determine the feasibility of using satellite data and classified UAV images to perform fractional cover mapping for the purpose of monitoring vegetation coverage over time.

2. Study Sites and Data

2.1. Study sites

The study area is comprised of three restoration sites located along the west coast of Western Australia (115.33o – 115.76oE, 31.03o – 32.5oS) within c. 115 km of Perth City (Figure 1). Each study site contained native vegetation that was previously cleared and subsequently revegetated prior to this study. Site rehabilitation footprints are small; Lancelin (Figure 1A), City Beach (Figure 1B) and Goegrup Reserve (Figure 1C) sites cover 0.54 ha, 0.26 ha and 0.1 ha, respectively. Lancelin was never revegetated but suffered vegetation loss because of an outfall overflow incident in April, 2021. Vegetation of the site consists of open shrubland of Myoporum insulare, Spyridium globulusum and Melaleuca cardiophylla over Lepidosperma gladiatum and Scaevola crassifolia with considerable presence of common lawn weeds. Another coastal site, City Beach, commenced revegetation in August, 2018. It is an open shrubland of Acacia rostellifera, S. globulusum and Oleria axillaris over L. gladiatum and S. crassifolia with low weed presence due to on-going weed management. The in-land Goegrup Reserve site was cleared in September, 2010 and revegetated around 2012. This site is an open wetland comprised of Eucalyptus species and Allocasuarina fraseriana over low shrubs of Melaleuca raphiophylla, Regelia ciliate and Jacksonia furcellata.

2.2. UAV Imagery Acquisition

Multispectral aerial imagery was collected for each site via a MicaSense RedEdge-P multispectral camera onboard a DJI –Matrice 300 RTK UAV. The RedEdge-P camera consists of a 1.6-megapixel (MP) resolution 5-band multispectral sensor capable of capturing: blue (475 nm), green (560 nm), red

Preprints (www.preprints.org) | NOT PEER-REVIEWED | Posted: 7 December 2023 doi:10.20944/preprints202312.0441.v1

(668 nm), red edge (717 nm) and near infrared (842 nm) wavelengths [13]. An additional red-green-blue (RGB) Zenmuse P1 camera (45 MP, 35 mm focal length; [14]) was fitted to the UAV and used to capture higher resolution RGB images to assist in identifying species during field work. The flight missions were performed autonomously using the DJI Pilot software. Flight altitude was fixed at 50 m altitude, and the average speed was 6 m.s-1. Images were captured every 1 second, and multispectral and RGB imagery was acquired at 3.8 cm and 0.3 cm spatial resolution, respectively. Flights were undertaken at Lancelin, City Beach and Goegrup Reserve sites under cloudless conditions between 10:00 and 12:00 (local time) on 15 November 2022, 15 February 2023, and 14 October 2022, respectively.

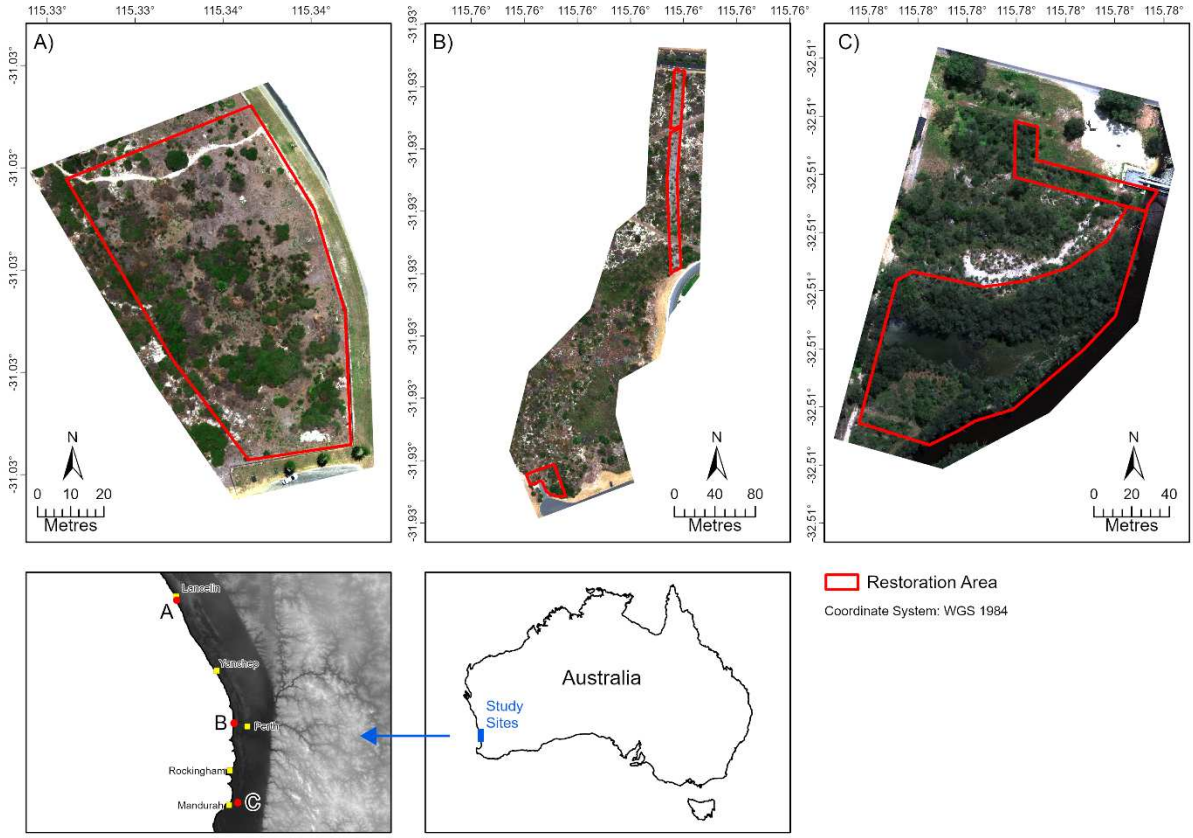

Figure 1. Locations of the three study sites: (A) Lancelin; B) City Beach; and (C) Goegrup Reserve. The red boundaries represent revegetation monitoring areas. Site images were captured between January and April, 2023 using a DJI Matrice 300 RTK UAV fitted with a MicaSense RedEdge-P multispectral camera (c. 3.8 cm spatial resolution).

2.3. Image Processing

2.3.1. UAV Image Pre-processing

An average of 3,500 multispectral and 500 RGB geotagged images were acquired per site by UAV and processed using the Pix4Dmapper software, version 4.8 [15]. Pix4Dmappers' standard "Ag Multispectral" processing model was used to generate orthomosaics of the individual spectra bands (blue, green, red, red-edge and near-infrared), and digital surface and terrain models (DSM and DTM, respectively) were automatically generated from the orthomosaic point clouds. Normalised DSMs were used to extract tree heights, which was used as an additional variable for classification.

Ground control points (GCPs) were not used at flight time, so we identified 12 prominent features at each site based on field observations and Google EarthTM to georeference mosaiced images [16]. The RedEdge-P multispectral imagery was radiometrically corrected for irradiance and sun angle in Pix4Dmapper using measurements captured by camera's on-board DLS2 light sensor and converted to reflectance using reference measurements provided by a field-based reflectance

 doi:10.20944/preprints202312.0441.v1

panel. Band mosaics and elevation images were exported as separate rasters in projected coordinate system WGS84 UTM Zone 50S.

2.3.2. Satellite Image Pre-processing

Sentinel-2 multispectral imagery was acquired from Digital Earth Australia (DEA) from the Analysis Ready Data (ARD) Collection 3 product [17]. This product offers standardised Sentinel-2 surface reflectance imagery corrected for atmospheric, radiometric and geometric issues based on a bi-directional reflectance distribution function (BRDF) with nadir and terrain illumination corrections (Li et al., 2010; 2012). For each site, we obtained one cloud-free Sentinel-2 multispectral image for each year from 2016 to 2023 that was nearest to the day and month of the site's UAV flight date (Table 1A). We acquired blue (490 nm), green (560 nm), red (665 nm), red edge 1 to 3 (705-740 nm), near-infrared-1 and -2 (842 and 865 nm) and SWIR-1 and -2 (1610 and 2190 nm) bands for each image using DEA web services [17]. All bands with 20 m spatial resolution were resampled to 10 m using nearest neighbour resampling by the DEA web service.

PlanetScope satellite images were also acquired at dates coinciding with the Sentinel-2 images. PlanetScope is a constellation of c. 130 satellites offering daily multispectral images at c. 3 m spatial resolution [11]. Using the Planet Explorer website (https://www.planet.com/explorer), we acquired one cloud-free image containing blue, green, red and near-infrared bands per year for the period 2018 to 2022 from the Dove Classic (Dove-C), Dove-R and Super Dove satellites (Table1B). Each image was provided pre-processed to bottom of atmosphere reflectance, and spectral bands were harmonised with Sentinel-2 reflectance values using the PlantScope 'harmonise' web option to ensure consistent radiometric compatibility between the different generations of PlanetScope satellites [18].

All Sentinel-2 and PlanetScope images were georectified to the same Google EarthTM imagery used to georectify the UAV imagery. We first reprojected all images to coordinate system WGS84 UTM Zone 50S. Then, we georectified one Sentinel-2 and Planet image manually per site and registered each unrectified raster to them using a "shift only" transformation in ArcGIS Pro [19]. Finally, we performed relative geometric correction on all Sentinel-2 and PlanetScope image sets per site. Relative correction requires that each image in a set is corrected relative to a reference image to minimise artefacts such as sun angles, haze and other atmospheric issues. We used histogram matching to achieve this, which matches the cumulative distribution functions from each image [20] where the reference image was set to the most recent image available for each satellite and study area.

2.4. Field Surveys and Sample Collection

Field surveys were conducted to record the locations and distribution of dominant and exotic species within restoration areas at each study site (Figure 1). Field investigations were carried out at the Goegrup, City Beach and Lancelin sites on 16 March 2023, 30 March 2023 and 9 August 2023, respectively. The locations of plant species were recorded using the ArcGIS Field Maps mobile app [21] running on a GPS-enabled Google Pixel 6 phone. To correct for ± 5 m GPS positioning inaccuracy, the georectified UAV RGB images were loaded as basemaps prior to the surveys and used to verify and correct GPS positions in the field. Species were identified in-field with a botanical expert present and further validated using photo and plant material assessments during a blind assessment conducted by a second botanist post-field. Infrequently observed species were noted but not recorded. Locations of other land cover types (e.g., tracks, sand, water) were recorded. Figure 2 presents a selection of dominant native and weed species encountered at each site.

 doi:10.20944/preprints202312.0441.v1

Table 1. Capture date and time of each (A) Sentinel-2 and (B) PlanetScope satellite image obtained from Digital Earth Australia and Planet Explorer web platforms for each study site. All images are used in fractional cover modelling.

			Site					
			Lancelin		City Beach		Goegrup	
	Platform	Year	Date Time1	Sat2	Date Time1	Sat2	Date Time1	Sat2
A.	Sentinel-2	2015	14 Nov 2:24	S2A	-	-	14 Nov 2:24	S2A
		2016	18 Nov 2:24	S2A	12 Feb 2:26	S2A	18 Nov 2:24	S2A
		2017	18 Nov 2:19	S2B	16 Feb 2:22	S2A	08 Nov 2:24	S2B
		2018	18 Nov 2:26	S2A	11 Feb 2:25	S2A	29 Oct 2:24	S2A
		2019	13 Nov 2:26	S2A	16 Feb 2:26	S2A	08 Nov 2:26	S2B
		2020	17 Nov 2:26	S2A	06 Feb 2:26	S2B	23 Oct 2:26	S2B
		2021	17 Nov 2:26	S2B	20 Feb 2:26	S2B	07 Nov 2:26	S2B
		2022	12 Nov 2:26	S2B	15 Feb 2:26	S2B	07 Nov 2:26	S2A
		2023	-	-	10 Feb 2:26	S2B	-	-
B.	PlanetScope	2015	-	-	-	-	-	-
		2016	10 Nov 1:34	DC	-	-	18 Oct 1:32	DC
		2017	21 Nov 1:43	DC	20 Jan 1:36	DC	14 Oct 1:39	DC
		2018	12 Nov 1:57	DC	12 Feb 1:45	DC	08 Oct 2:56	DC
		2019	15 Nov 2:21	DR	14 Feb 2:37	DC	12 Oct 2:00	DC
		2020	24 Nov 2:24	DR	13 Feb 2:24	DR	11 Oct 2:36	DR
		2021	15 Nov 3:00	DR	12 Feb 2:42	DR	16 Oct 1:32	SD
		2022	14 Nov 2:02	SD	09 Feb 2:58	DR	16 Oct 1:25	SD
		2023	-	-	16 Feb 1:56	SD	-	-

1Time in UTC; 2S2A: Sentinel 2A, S2B: Sentinel 2B, DC: Dove Classic, DR: Dove R, SD: Super Dove.

Following field collection, we used ArcGIS Pro to digitise ≥ 30 circular region of interest (ROI) polygons, each 50 cm in diameter, per species and land cover class using the ground truthed observations as reference. This ensured that ≥ 3,000 pixels were available per class for classification; at least twice as many as recommended by Mather (2004). Additionally, numerous smaller ROI areas were used to reduce potential mixed pixel issues (see [22]). A total of 1,849, 1,212 and 1,339 ROI samples were digitised at Lancelin, City Beach and Goegrup sites, respectively. A complete species inventory and further information about ROI data are provided in Appendix A for the Lancelin (Figure A1), City Beach (Figure A2) and Goegrup (Figure A3) sites.

Preprints (www.preprints.org) | NOT PEER-REVIEWED | Posted: 7 December 2023 doi:10.20944/preprints202312.0441.v1

Figure 2. Examples of dominant native and exotic species observed at each study site. (A) Scaevola crassifolia, (B) Olearia axillaris and (C) common lawn weeds (e.g., *Poa annua, *Gazania linearis) at Lancelin, respectively. City Beach contained natives (D) Acacia rostellifera and (E) Lepidosperma gladiatum, and exotic (F) *Pelargonium capitatum. Goegrup contained natives (G) Allocasuarina fraseriana, (H) Jacksonia furcellata, and exotics (I) *Avena barbata and *Lagurus ovatus.

3. Methods

The methodology used in this study consists of three broad stages: (1) pixel-based classification of native and exotic species at species- and broad-level groups using spectral, vegetation, texture, and canopy height images derived from multispectral UAV imagery; (2) fractional cover modelling of native and exotic broad-level groups using classified UAV, coincident satellite imagery and ordinary least squares and geographically weighted regression techniques; and (3) time-series based linear and quadratic trend analysis of fractional images. Figure 3 provides an overview of the process.

Preprints (www.preprints.org) | NOT PEER-REVIEWED | Posted: 7 December 2023 doi:10.20944/preprints202312.0441.v1

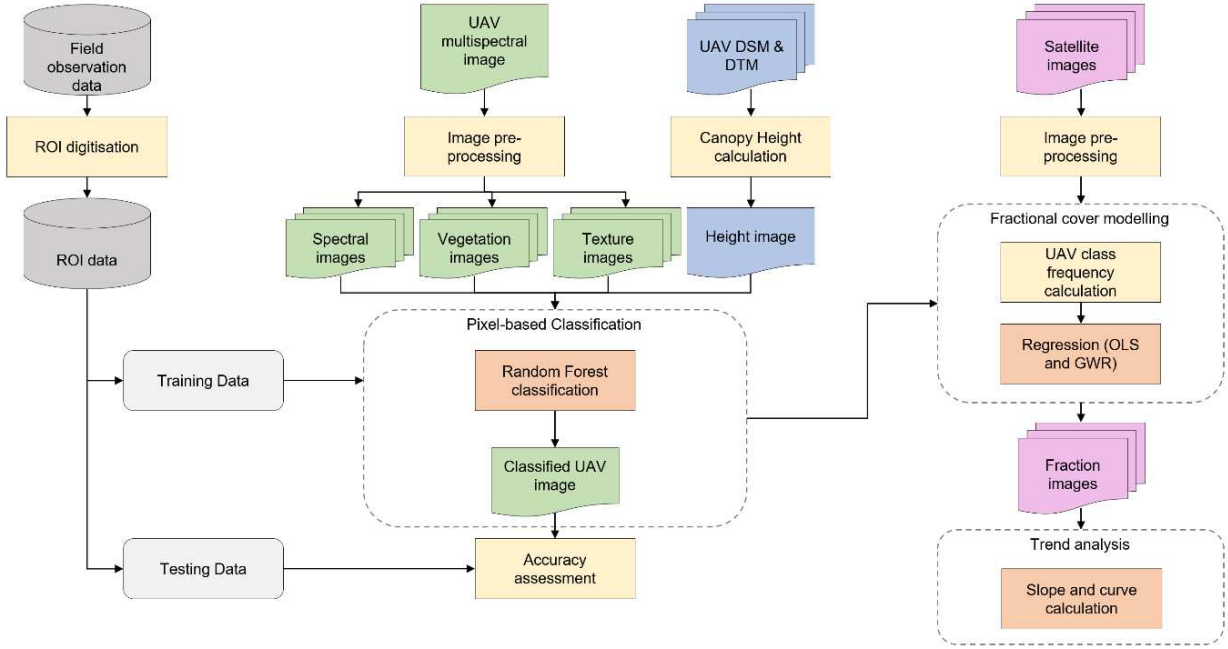

Figure 3. Flowchart of methodology used for classification of multispectral UAV imagery and its combination with multispectral Sentinel 2 and Planet satellite imagery in fractional cover modelling and trend analysis. This workflow was applied at each study site.

3.1. UAV Image Classification

3.1.1. Image-derived Variables

Classification accuracy has been demonstrated to improve where spectral overlap between species occurs, by including ancillary information such as vegetation indices, textural and height information [23]. In this study, four types of ancillary data were evaluated and used in classification (Table 2). (1) Five spectral reflectance bands captured by the UAV were considered. (2). Five vegetation indices (VIs) common in previous studies (e.g., [24,25]) were also derived from UAV imagery. These included the normalised green-red difference index (NGRDI; [26]), red-green-blue vegetation index (RGBVI; [27]), normalised difference red edge index (NDREI; [28]), normalized difference vegetation index (NDVI; [29]), and optimized soil adjusted vegetation index (OSAVI; [30]). (3) Textural images have been used in both pixel-based classification studies due to their ability to represent local spatial and tonal variations in an image [31,32]. A popular statistical method for extracting textural information from grayscale imagery is the grey-level co-occurrence matrix (GLCM; [33]). Based on Mohammadpour et al. [34], we first applied a principal component analysis (PCA) to each UAV image, extracted the first principal component band and converted to grayscale using ArcGIS Pro to generate GLCM. From each GLCM, we calculated eight second-order texture images including angular second moment (ASM), contrast (CON), correlation (COR), dissimilarity (DIS), entropy (ENT), mean (MEAN) and standard deviation (STDV) using a 5x5 cell window and default settings using the glcm package [35] in R software [36]. Additionally, we calculated six first-order texture images without the GLCM based on Anys et al. [37] including kurtosis (KURT), maximum (MAX), minimum (MIN), range (RNG), skew (SKEW) and variance (VAR) using focal statistics with a 5 x 5 window in ArcGIS Pro. (4) For each site, the UAV-derived DTM was subtracted from the DSM image to obtain a canopy height model (CHM) based on Matese et al. [38]. The CHM provides relative height information of vegetation with respect to ground.

We determined the optimal sets of variables that can discriminate between species observed using Variable Importance in the Projection (VIP; [39]) scores. A VIP score ≤ 1 indicates a variable is

Preprints (www.preprints.org) | NOT PEER-REVIEWED | Posted: 7 December 2023 doi:10.20944/preprints202312.0441.v1

less likely to differentiate between species and may be excluded from classification. We generated 10 random points within each ROI polygon and extracted pixel values of every variable at each. These were used to calculate VIP for both species- and broad-level groups per site using the pls package in R [40].

3.1.2. Classification and Validation

UAV images were classified using pixel-based classification. This approach assumes individual pixels are independent and thus treated without consideration of their spatial association with neighbours [41]. While this approach is prone to a "salt and pepper" effect [42], it does not require pre-processing segmentation and feature optimisation like object-based image analysis [43]. To classify species and land cover at our sites, we used Random Forest (RF), a non-parametric technique based on classification and regression trees (CART). According to Breiman [44], RF operates by generating an arbitrary number of decision trees at training time via bootstrap samples. Approximately one third of the overall sample is set aside for validation, and the tree is split using a randomised subset of the predictor variables at each tree node. When used for classification tasks, the output of the random forest is the class selected by most trees. We chose RF due to its performance in comparable studies (e.g., [31,45,46]) as well as its insensitivity to outliers and its processing efficiency ([47]).

For each study site, two groups of ROIs were considered for the classification. The first group contained ROIs with classes representing individual species (i.e., species-level), while the other grouped species into broad "native" and "exotic" classes (i.e., "broad-level"). In both groups, all land-cover classes were combined into a single "other" class. For each group, stratified random sampling was used to split ROIs into 50% training and 50% validation sets of equal size per class. This random selection process was undertaken five times for each group, creating ten cross-validation ROI sets per study site [16]. We performed ten random forest classifications using the Spatial Analyst extension in ArcGIS Pro with default settings with the exception that tree number (ntrees) was increased to 1000 trees. For each iteration, the ROI training sets were used as training features in the classifier, and the UAV reflectance images and derivatives as explanatory variables.

Table 2. Overview of multispectral UAV derivatives used in classification. Broad types of derivatives include (A) spectral UAV bands; (B) vegetation indices (VIs); (C) first-order textural indices; (D) grey-level co-occurrence matrix (GLCM) second-order textural images; and (E) canopy height model (CHM). Equations and references are provided for each where applicable.

	Variable Type	Variable	Description	Equation	Reference
A.	Spectral bands (reflectance)	B	Blue band	N/A	N/A
		G	Green band		
		R	Red band		
		RE	Red edge band		
		NIR	Near-infrared band		
B.	Vegetation index	NGRDI	Normalised Green-Red Difference Index	$\frac{G-R}{G+R}$	[26]
		RGBVI	Red-Green-Blue Vegetation Index	$\frac{G^2-R\times B}{G^2+R\times B}$	[27]
		NDREI	Normalised Difference Red Edge Index	$\frac{NIR-RE}{NIR+RE}$	[28]
		NDVI	Normalized Difference Vegetation Index	$\frac{NIR-R}{NIR+R}$	[29]
		OSAVI	Optimized Soil Adjusted Vegetation Index	$\frac{(NIR-R)(1+0.16)}{NIR+R+0.16}$	[30]
C.	Textural image (first-order)	KURT	Kurtosis	$\sum_{i=0}^{n-1}(i-\bar{x})^4 P_i$	[37]
		MAX	Maximum	$\sum_{i=0}^{n-1} max(P_i)$	
		MIN	Minimum	$\sum_{i=0}^{n-1} min(P_i)$	

Preprints (www.preprints.org) | NOT PEER-REVIEWED | Posted: 7 December 2023 doi:10.20944/preprints202312.0441.v1

		RNG	Range	$\sum_{i=0}^{n-1} max(P_i) - \min(P_i)$	
		SKEW	Skew	$\sum_{i=0}^{n-1} (i-\bar{x})^3 P_i$	
		VAR	Variance	$\sum_{i=0}^{n-1} (i-\bar{x})^2 P_i$	
D.	Textural image (second-order)	ASM	Angular Second Moment	$\sum_{i,j=0}^{n-1} P_{i,j}^2$	[33]
		CON	Contrast	$\sum_{i,j=0}^{n-1} P_{i,j}(i-j)^2$	
		COR	Correlation	$\sum_{i,j=0}^{n-1} P_{i,j}\left[\frac{(i-\mu_i)(i-\mu_j)}{\sqrt{(\sigma_i^2)(\sigma_j^2)}}\right]$	
		DIS	Dissimilarity	$\sum_{i,j=0}^{n-1} P_{i,j}\lvert i-j\rvert$	
		ENT	Entropy	$\sum_{i,j=0}^{n-1} P_{i,j}(-\mathrm{In}\, P_{i,j})$	
		HOM	Homogeneity	$\sum_{i,j=0}^{n-1} \left(\frac{P_{i,j}}{1+(i-j)^2}\right)$	
		MEAN	Mean	$\sum_{i,j=0}^{n-1} i(P_{i,j})$	
		STDV	Standard Deviation	$\sum_{i,j=0}^{n-1} P_{i,j} - \mu^2$	
E.	Height image	CHM	Canopy Height Model	$DSM - DTM$	[38]

Potential noise known as the salt-and-pepper effect often associated with pixel-based classification was reduced by applying a 5 x 5 cell median filter [48]. To assess accuracy of random forest classification results, and to evaluate the effectiveness of using UAV multispectral data in species classification, confusion matrices were generated using the associated validation ROI set. For each iteration, the confusion matrix was used to calculate the overall accuracy (OA) and Kappa index of agreement to assess overall accuracy, and the user's accuracy (OA) and producer's accuracy (PA) to assess specific class accuracy [49]. The average of all metrics is presented.

3.2. Fractional Cover Mapping

Fractional cover mapping typically involves several steps including the estimation of class cover represented as a percentage (e.g., canopy cover percent) obtained from field-based plot samples, aggregation of field estimates to a raster with a cell resolution equal to Xn predictor variables, and then the prediction of Yn via global regression or linear spectral unmixing algorithms [50]. In this study, we estimated the subpixel native, exotic and other class fractions using a novel six step data-driven approach using ArcGIS Pro. (1) Each geometrically and radiometrically corrected Sentinel-2 and PlanetScope satellite image (see Table 1) overlayed with the UAV image for each site. (2) Pixels from satellite images were converted into polygons to create a sampling grid, where polygon size was identical to pixel size (10 m^2 and 3 m^2 for Sentinel 2 and PlanetScope, respectively). (3) Within each polygon we calculated the total number of classified UAV pixels representing either native, exotic and other land cover and divided by the pixel total to obtain class fractions. This resulted in c. 62,000 and c. 3,600 classified pixels per polygon for Sentinel 2 and PlanetScope imagery, respectively. Any polygons containing empty pixels were removed. (4) Fraction grids were duplicated for each satellite image, and satellite band reflectance values were extracted at each polygon for use as predictor variables during modelling (Xn). (5) An OLS and GWR model were built for each native, exotic and other class for each satellite image using the predictor variables.

GWR models were trained using a random selection of 75% of the available fraction polygons, and the remaining 25% was used for model validation. We used a Gaussian model type with a distance band bandwidth to enforce a constant neighbourhood size as our samples were spatially uniform [51]. The size of the bandwidth was selected using a Golden search, which allows the model to determine optimal distance (Fotheringham et al., 2003). We also built global ordinary least squares (OLS) regression model simultaneous to each GWR model to the localised GWR technique. OLS and GWR goodness of fit was measured using the coefficient of determination (R^2) and models were compared via the corrected Akaike Information Criterion (AICc; [52]).

3.3. Trend Analysis

We converted the temporal fractional cover models to three-band RGB (red, green, blue) trend rasters to explore rehabilitation condition change over time. We based our approach on the

Preprints (www.preprints.org) | NOT PEER-REVIEWED | Posted: 7 December 2023 doi:10.20944/preprints202312.0441.v1

"Vegetation Trend" product produced by the Land Monitor II Project [53], which computes trends through equally-spaced time-series data based on the linear trend and the curvature (quadratic component) using orthogonal polynomial coefficients [54]. For the linear trend information, increasing (positive) slope values were isolated and assigned to the blue band, decreasing (negative) slope values were assigned to the red band. Additionally, positive curvature values were assigned to the green band. When visualised, the colours displayed on a given RGB trend composite may correspond to one of the trend types shown in Table 3.

Table 3. Interpretation of the colours associated with a RGB trend composite, based on Robinson et al. [55].

Colour	Interpretation
Red	Continuous loss over time.
Green	Recent gain (last few years) after period of loss. Recent gain typically back to original or higher levels.
Blue	Continuous gain over time.
Yellow	Recent gain (last few years) after period of loss. Recent gain not up to original levels.
Cyan	Continuous gain over time, with highest gains recently (last few years).
Black	No significant gain or loss (stable). Can be stable high or low values.
White	Not possible.
Magenta	Not possible.

4. Results

4.1. UAV Image Classification

4.1.1. UAV Image-derived Variables

Seven variables were found to significantly differentiate between classes in both the broad- and species-level tests, based on the observed VIP score ≥ 1 (Table 4). These included spectral reflectance RGB and NIR bands and vegetation indices NDREI, NDVI and OSAVI. The RE (red edge) band and most first-order texture variables were unhelpful in discriminating between classes (VIP < 1). Second-order texture variables generally performed better than first-order variables, though were still relatively inconsistent across tests. Broad-level models benefited from the inclusion of ENT and STDV (VIP ≥ 1), while ASM was discriminable in species-level models at City Beach and Goegrup. No other texture variables were helpful. Canopy height (CHM) discriminated well at sites where a higher variation in species height was observed (i.e., Lancelin and Goegrup).

Table 4. UAV Image-derived variables and Variable Importance in the Projection (VIP) scores calculated for the three study sites. The VIP scores were obtained for broad- and species-level region of interest groups. The values highlighted grey represent variables that significantly differentiated between classes (i.e., VIP above the ≥ 1 rejection threshold).

			VIP Score					
			Lancelin Site		City Beach Site		Goegrup Site	
	Variable Type	Variable	Broad	Species	Broad	Species	Broad	Species
A.	Spectral bands (reflectance)	B	1.22	1.09	1.63	1.42	1.16	1.05
		G	1.21	1.11	1.51	1.30	1.19	1.08
		R	1.02	1.06	1.43	1.48	1.18	1.09
		RE	0.98	0.71	0.88	0.91	0.07	0.16
		NIR	1.35	1.03	1.12	1.03	1.01	1.07
B.	Vegetation index	NGRDI	0.70	1.57	0.46	1.31	1.14	0.79
		RGBVI	0.86	1.68	0.87	1.44	1.40	1.13
		NDREI	1.55	1.62	1.44	1.43	1.29	1.01

Preprints (www.preprints.org) | NOT PEER-REVIEWED | Posted: 7 December 2023 doi:10.20944/preprints202312.0441.v1

		NDVI	1.16	1.61	1.45	1.56	1.56	1.19
		OSAVI	1.16	1.61	1.43	1.50	1.66	1.36
C.	Textural image (first-order)	KURT	0.16	0.15	0.08	0.04	0.04	0.08
		MAX	1.42	0.88	0.03	0.31	1.12	0.85
		MIN	1.28	0.76	0.42	0.54	1.02	0.52
		RNG	0.82	0.62	0.96	0.51	0.86	0.97
		SKEW	0.01	0.02	0.03	0.04	0.04	0.03
		VAR	0.53	0.42	0.63	0.31	0.58	0.87
D.	Textural image (second-order)	ASM	0.64	0.38	1.02	0.50	0.78	1.15
		CON	0.36	0.31	0.64	0.30	0.54	0.97
		COR	0.33	0.24	0.57	0.31	0.53	0.62
		DIS	0.52	0.41	0.74	0.35	0.63	0.98
		ENT	1.01	0.47	1.03	0.48	1.03	1.25
		HOM	0.56	0.42	0.76	0.36	0.64	0.99
		MEAN	1.25	0.71	0.16	0.37	0.98	0.98
		STDV	1.04	0.44	1.03	0.43	1.03	0.97
E.	Height image	CHM	1.62	1.12	0.31	0.63	1.01	1.08

1 ROIs grouped into classes comprising natives, exotics and other. 2 ROIs grouped into species-level classes.

4.1.2. Classification and Validation

Table 5 summarises the classification accuracy results (see Appendix B for full confusion matrices). When trained using species-level data, we achieved an overall accuracy and Kappa coefficient greater than 70% and 0.7 at all study sites, respectively (Table 5A). According to Landis and Koch [56], a Kappa value between 0.6 and 0.8 equate to a substantial reliability for all sites. Accuracy improved considerably when three broad-level classes (i.e., native, exotic and other land cover) were used, resulting in an overall accuracy and Kappa coefficient greater than 90% and 0.9 across all study sites, respectively (Table 5B). This represents an almost perfect reliability [56]. Low PA and UA across Lancelin were found for species *M. insulare*, *A. preissii*, **G. fruiticosus*, *A. lehmanniana* (light) and *Lawn weeds (Table 5A). *A. elegantissima* and *S. globulosum* also showed low PA (63.2% and 62.4%, respectively). *S. globulosum* was also found to have low PA and UA at City Beach, along with *C. quadrifidus*, *G. preissii*, and *M. cardiophylla*. Species with low PA included *T. retusa* (44.4%), *M. huegelii* (61.1%) and *A. lehmanniana* (63.3%), while *R. baccata* had a low UA of 62.6% (Table 5A). The dominant exotic (**P. capitatum*) classified well at City Beach. Species observed a generally higher PA and UA overall at Goegrup Reserve. Considerably low PA and UA was observed for several exotics including **A. barbata*, **L. ovatus* and **A. calendula* (Table 5A). While PA was generally high for the remaining species, UA was low for *L. caespitosa* (53.7%). For broad-level classification, PA and UA was consistently high (≥ 90%) for native, exotic and other land cover classes across all sites (Table 5B). Figure 4 presents a sub-section of the species-level (Figure 4A) and broad-level (Figure 4B) classification map at the City Beach site where a mixture of native and exotic (**Pelargonium capitatum*) were observed. Appendix C provides classification maps for species- and broad-level ROIs for each site.

4.2. Fractional Cover Mapping

Higher accuracy was achieved in every instance when GWR (native R2 = 0.56-0.78, exotic R2 = 0.54-0.69) was used to model broad-level native and exotic fraction class data compared to OLS (native R2 = 0.26-0.56, exotic R2 = 0.16-0.36; Table 6). Furthermore, average accuracy of GWR-based native and exotic fractional cover maps improved when higher-resolution (3 m) Planet imagery predictors were used compared to moderate-resolution Sentinel-2 (10 m), with the only exception being City Beach exotic fractions (Table 6). However, the inverse of this is true when OLS is compared between satellites, with Planet-based OLS models underperforming compared to Sentinel-2 OLS models in almost every instance (Table 6). For each GWR model, the observed range of R2 values was

Preprints (www.preprints.org) | NOT PEER-REVIEWED | Posted: 7 December 2023 doi:10.20944/preprints202312.0441.v1

mostly lower when compared to the associated OLS R2 range, suggesting the GWR method offered more consistent model performance. According to Miles [57], R2 is a measure of goodness of fit, with values closer to 1.0 representing a stronger, preferable model. However, as Sentinel-2 models contained more explanatory variables (i.e., bands) than Planet imagery (10 and 4, respectively), the potential to observe inflated R2 for Sentinel-2 models exists [57]. As such, the AICc, which is helpful for comparing model performance between global (e.g., OLS) and local (e.g., GWR) regression models with differing exploratory variables [58], was calculated and provided in Appendix D Table D1. In every instance, the AICc of GWR models was lower than its associated OLS model, reinforcing that the local GWR technique improved fractional cover mapping.

Table 5. Classification validation results with producer's accuracy (PA), user's accuracy (UA), percent overall accuracy, and Kappa for Lancelin, City Beach and Goegrup study sites. Validation measurements provided for classification undertaken with (A) species-level ROIs and (B) broad-level ROIs grouped into native, exotic and other classes.

		Lancelin Site			City Beach Site			Goegrup Site		
Dataset		**Class**	**PA**	**UA**	**Class**	**PA**	**UA**	**Class**	**PA**	**UA**
A.	Species-level	A. cyclops	87.2	89.5	A. cyclops	73.3	73.3	*A. barbata	30.5	33.3
		A. elegantissima	63.2	80.4	A. elegantissisma	86.7	78.8	*A. calendula	62.1	57.3
		A. flexulosa	68.4	70.8	A. lasiocarpa	64.4	76.3	A. flexuosa	89.5	97.7
		A. lehmanniana (dark)	74.4	81.3	A. lehmanniana	63.3	69.5	A. fraseriana	92.6	88.9
		A. lehmanniana (light)	59.0	65.7	A. preissii	82.2	85.1	*B. maxima	91.6	88.8
		A. preissii	60.7	56.8	A. rostellifera	58.9	71.6	C. calophylla	85.3	97.6
		*E. villosa	69.2	87.1	C. quadrifidus	51.1	49.5	*C. dactylon	70.5	69.8
		*G. fruticosus	59.0	61.1	E. sp. huge leaves	97.8	94.6	E. gomphocephala	82.1	86.7
		*Lawn Weeds	65.0	61.3	F. nodosa	88.9	67.8	E. rudis	87.4	75.5
		L. gladiatum	86.3	81.5	G. preissii	61.1	49.5	G. trifida	81.1	75.5
		M. cardiophylla	76.1	67.4	L. gladiatum	74.4	68.4	H. comptoniana	88.4	94.4
		M. insulare	61.5	41.4	M. cardiophylla	63.3	62.6	J. furcellata	68.4	77.4
		O. axillaris	94.9	95.7	M. huegelii	61.1	68.8	J. kraussii	65.3	81.6
		Other	94.9	97.4	M. lanceolata	78.9	67.6	L. caespitosa	69.5	53.7
		Red Moss sp.	100	93.6	O. axillaris	96.7	93.5	*L. ovatus	42.1	54.8
		S. crassifolia	70.9	76.1	Other	98.9	100	M. fraseri	85.3	73.6
		S. globulosum	62.4	67.0	*P. capitatum	83.3	92.6	M. juncea	65.3	67.4
					R. baccata	80.0	62.6	M. rhaphiophylla	76.8	76.8
					S. crassifolia	75.6	78.2	Other	89.5	89.5
					S. globulosum	45.6	47.1	R. ciliata	71.6	74.7
					S. longifolia	71.1	85.3	T. pergranulata	95.8	81.3
					T. retusa	44.4	71.4			
		Overall Accuracy (%)	73.7			72.8			75.7	
		Kappa	0.72			0.71			0.74	
B.	Broad-level	Native	91.9	91.2	Native	94.7	96.2	Native	90.1	91.9
		Exotic	88.1	92.1	Exotic	95.5	97.1	Exotic	92.9	92.8
		Other	98.1	94.7	Other	99.7	96.7	Other	97.1	95.3
		Overall Accuracy (%)	92.7			96.6			93.3	
		Kappa	0.90			0.95			0.91	

Preprints (www.preprints.org) | NOT PEER-REVIEWED | Posted: 7 December 2023 doi:10.20944/preprints202312.0441.v1

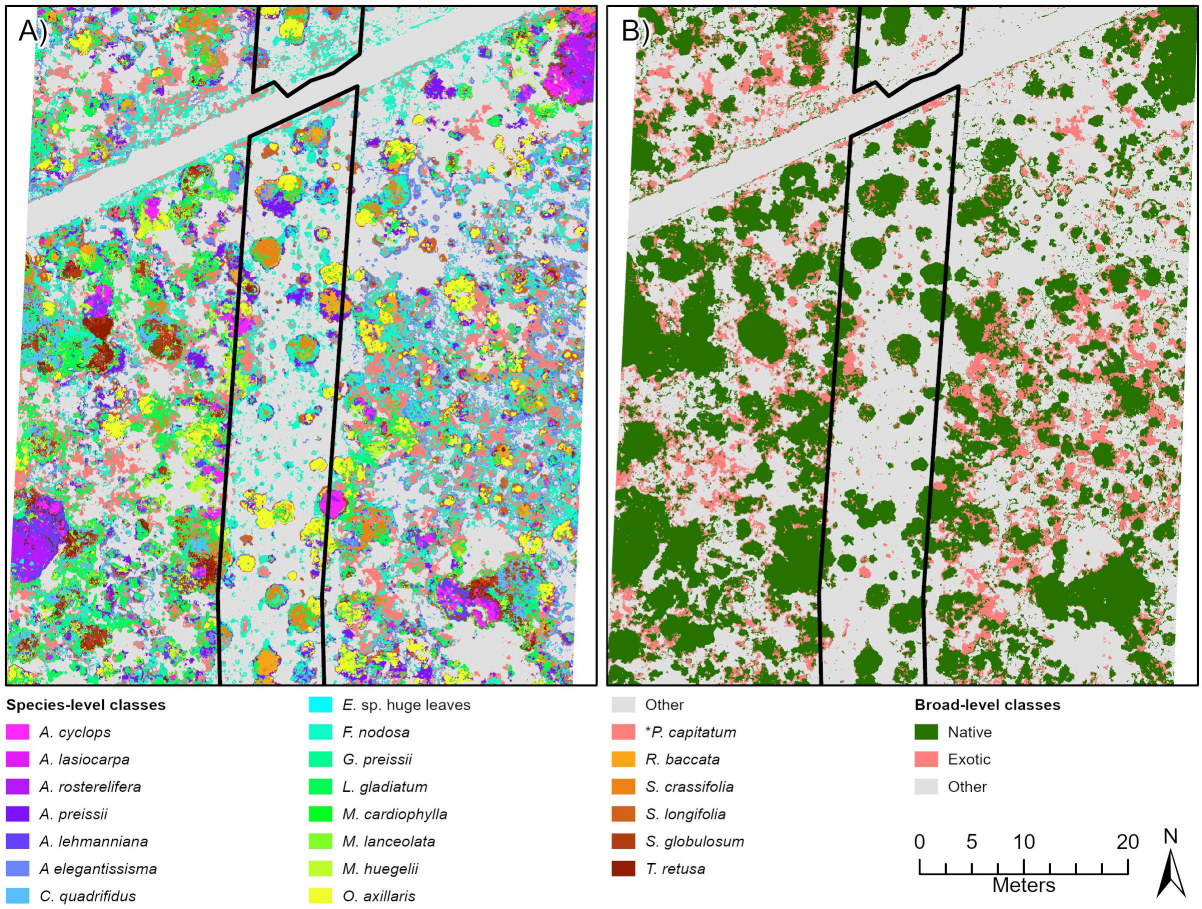

Figure 4. Classification outputs based on species-level (A) and broad-level (B) training ROIs for a sub-section of the City Beach site. This location shows an area of the site where many native and exotic (*Pelargonium capitatum) species were observed occurring together.

4. Discussion

Our results demonstrate the ability of standard drone imagery to detect individual plants and discriminate between broad species classes, as established by Gomez-Sapiens et al. [9]. However, the assessment of native vegetation recovery and factors that can curtail reestablishment of biodiversity such as weed invasion require repeat acquisitions. Satellite remote sensing is a more convenient method for adding this temporal component [10] but has either been too expensive or of an unacceptable spatial resolution to provide useful information at the plot scale [8]. We investigate the applicability of freely available Sentinel imagery at 10 m resolution and low-cost, 3 m, imagery from Planet's Dove and Superdove satellites for estimating the proportion of exotic and native species within each pixel using fractional cover mapping. When collected over time, this provides the ability to identify vegetation cover trends including exotic weed expansion and native vegetation trajectory [12].

Preprints (www.preprints.org) | NOT PEER-REVIEWED | Posted: 7 December 2023 doi:10.20944/preprints202312.0441.v1

Table 6. R-Squared values produced from the fractional cover modelling procedure based on Ordinary Least Squares (OLS) and Geographically Weighted Regression (GWR) techniques. Both methods were applied to Sentinel-2 and PlanetScope images over the period 2015 to 2023 at Lancelin, City Beach and Goegrup study sites.

		Lancelin Site				City Beach Site				Goegrup Site			
		Sentinel-2		Planet		Sentinel-2		Planet		Sentinel-2		Planet	
	Year	OLS	GWR	OLS	GWR	OLS	GWR	OLS	GWR	OLS	GWR	OLS	GWR
Natives Fractions	2015	0.42	0.60	-	-	-	-	-	-	0.62	0.70	-	-
	2016	0.43	0.45	0.19	0.53	0.39	0.58	-	-	0.59	0.69	0.34	0.77
	2017	0.40	0.52	0.20	0.50	0.31	0.61	0.33	0.59	0.51	0.71	0.43	0.78
	2018	0.34	0.56	0.18	0.57	0.33	0.60	0.30	0.60	0.56	0.76	0.43	0.79
	2019	0.42	0.61	0.26	0.55	0.34	0.59	0.40	0.64	0.57	0.72	0.45	0.78
	2020	0.37	0.58	0.29	0.61	0.36	0.59	0.42	0.66	0.55	0.71	0.46	0.81
	2021	0.45	0.62	0.33	0.63	0.36	0.61	0.40	0.63	0.48	0.72	0.34	0.77
	2022	0.49	0.65	0.34	0.65	0.47	0.63	0.50	0.68	0.62	0.75	0.47	0.79
	2023	-	-	-	-	0.50	0.61	0.43	0.63	-	-	-	-
	Mean	0.41	0.57	0.26	0.58	0.38	0.60	0.40	0.63	0.56	0.72	0.42	0.78
	Range	0.15	0.17	0.16	0.13	0.16	0.05	0.20	0.09	0.14	0.07	0.13	0.04
Exotic Fractions	2015	0.36	0.56	-	-	-	-	-	-	0.27	0.59	-	-
	2016	0.34	0.52	0.12	0.58	0.30	0.67	-	-	0.31	0.57	0.23	0.63
	2017	0.41	0.58	0.20	0.56	0.32	0.68	0.18	0.59	0.29	0.48	0.17	0.64
	2018	0.32	0.54	0.15	0.53	0.36	0.69	0.14	0.60	0.33	0.52	0.19	0.63
	2019	0.39	0.55	0.22	0.61	0.34	0.70	0.17	0.61	0.32	0.51	0.17	0.63
	2020	0.44	0.52	0.34	0.65	0.38	0.69	0.15	0.62	0.33	0.61	0.21	0.66
	2021	0.34	0.54	0.26	0.59	0.34	0.69	0.16	0.59	0.34	0.60	0.25	0.67
	2022	0.29	0.53	0.13	0.59	0.39	0.71	0.15	0.63	0.35	0.62	0.16	0.66
	2023	-	-	-	-	0.40	0.71	0.15	0.60	-	-	-	-
	Mean	0.36	0.54	0.20	0.59	0.35	0.69	0.16	0.61	0.32	0.56	0.20	0.64
	Range	0.15	0.06	0.22	0.12	0.09	0.04	0.04	0.04	0.08	0.14	0.09	0.04

We used raw spectral bands, vegetation indices, textural images, and vegetation height as input into classification as done by Wilson et al. [59]. Significantly important variables were identified reoccurring across sites and included spectral bands (n = 4) and vegetation indices (n = 3). Spectral bands and vegetation indices are prevalent in image classification, and our findings reflect satellite-based (e.g., [60,61]) and UAV-based (e.g., [16,23]) studies. The red-edge band was not useful at any of the three sites. This is in line with the results of Pu and Cheng [62] for mapping mixed forest, and Darvishzadeh et al. [63] for estimating leaf area index of structurally different plants with different soil backgrounds and leaf optical properties. However, many other studies have found the red-edge to be essential for discriminating between species of varying health (e.g. [64,65]) and for mapping mangrove forests (e.g. [66]). Hence, its value in classification appears to depend on how much coexisting or target vegetation varies around 700-750 nm.

Preprints (www.preprints.org) | NOT PEER-REVIEWED | Posted: 7 December 2023 doi:10.20944/preprints202312.0441.v1

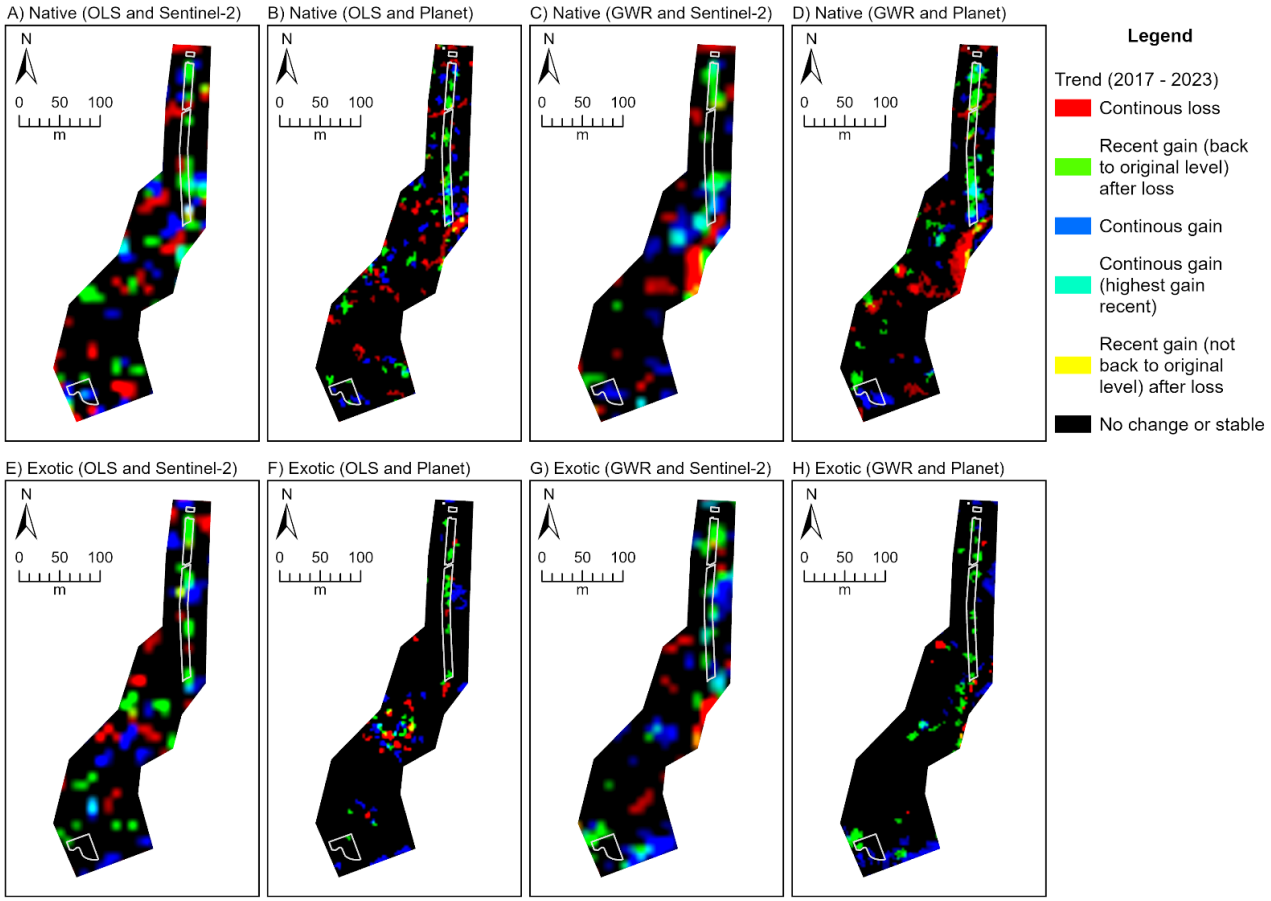

Figure 5. Three band RGB (red, green, blue) trend rasters depicting rehabilitation condition change every February over the period 2017 to 2023 at the City Beach site. Trends are derived from temporal fractional models representing natives (A-D) and exotics (E-H). Trend rasters produced from the Sentinel-2 (A, C, E, G) and Planet (B, D, F, H) fraction models and ordinary least squares (OLS; A, B, E, F) and geographically weighted regression (GWR; C, D, G, H) techniques are provided. See Appendix E for the trend outputs for Lancelin and Goegrup sites.

A majority (n = 8) of textural variables were found to be unimportant across sites. Those that were important (n = 6) were mostly only helpful when native and exotic species were generalised into broad-level classes. Studies using pixel-based classification have successfully applied texture imagery to improve classification accuracy (e.g., [34, 68, 69]). However, these are usually undertaken at a regional scale or consider fewer classes than observed at local-scale revegetation sites. Like Wilson et al. [59], our findings indicate that textural images may not provide enough information to adequately separate classes at the species-level when using high-resolution imagery.

Comparison of Kappa between sites showed that differing species diversity and revegetation age did not considerably influence classification accuracy. For example, Lancelin and City Beach sites obtained very comparable Kappa (0.72 and 0.71, respectively) despite Lancelin's older and lower species diversity (n = 17) compared to City Beach's less established (c. 5 years) and higher diversity (n = 22). Increased species diversity can reduce a classifier's ability distinguish between large numbers of visually similar classes, impacting both Kappa and increasing class confusion (e.g., [70,59]). Assessment of the PA and UA and confusion matrices (see Appendix B) of plant species indicated that various native mid-storey shrubs were highly confused at the Lancelin and City Beach sites. At Lancelin, the native shrub M. insulare was highly confused with S. crassifolia, M. cardiophylla and A. lehmanniana, all of which are native shrubs of similar height, spreading growth form and dull green leaf colour [71,72,73,74]. Likewise, at City Beach, confusion occurred between various native shrubs including S. globulosum, C. quadrifidus, T. retusa and G. preissii, all of which have similar branching and dark chlorophyl [75,76,77,78]. Exotic species were comprised entirely of

 doi:10.20944/preprints202312.0441.v1

low-lying herbs and grasses and were also often confused with other exotics. *G. frutocosus, an erect perennial herb, was misclassified as other common lower-lying herbs represented in the *Lawn Weeds class despite a paler complexion [79] at Lancelin, while the co-occurring erect annual grasses *A. barbata and *L. ovatus, were highly confused at the City Beach site [80,81]. Confusion between native and exotic species was minimal, with the exception A. elegantissima, a rhizomatous perennial grass [82], sometimes being omitted from its true *G. fruticosus class, at Lancelin. Being that the separation between natives and exotics is between mid-storey shrubs and low-lying exotic herbs and grasses, it is suggested canopy height is included to ensure the classifier can consider this separation [83].

Confusion between plant species in species-diverse landscapes is a common issue in machine-learned classification of high-resolution imagery (e.g., [70,84,59]). For pixel-based classification, confusion may occur when subtle variation in spectral reflectance between species, such as the vivid green pigmentation of M. insulare and the greyish-green hue of A. lehmanniana, is too fine to be measured by course multispectral UAV sensors [85]. Literature applying machine learning to classify vegetation has reduced class confusion and improved classification accuracy by grouping confused species into one class (e.g., [70]), broader plant communities or type (e.g., [86]), or by combing species into native and exotic classes (e.g., [87]). Grouping similar species such as M. insulare, S. crassifolia and M. cardiophylla into a single class may still provide information for on-going vegetation monitoring whilst improving classification accuracy. For example, significant improvements to classification accuracy were seen at all sites (Kappa ≥ 0.9) when species were aggregated into broad native and exotic classes. Other studies have improved species discrimination by using UAV-fitted hyperspectral sensors to increase spectral resolution (e.g., [23,88]). However, due to the higher cost associated with hyperspectral sensors and the need for additional processing due to increased image dimensionality, their uptake is still relatively low compared to multispectral UAV sensors [89].

Noise in the form of the "salt-and-pepper" effect was observed at various canopies and canopy edges (e.g., A. cyclops and A. rostellifera at City Beach). This phenomenon is often associated with pixel-based classification and is caused by high local spatial heterogeneity between neighbouring pixels within the same land surface (e.g., a tree canopy). As each pixel is classified in isolation without consideration for surrounding pixels, spectrally similar neighbours may be assigned to different classes, often leading to a reduction in species-level classification accuracy [90,91]. While the application of a majority filter can successfully reduce the noise effect [92], many studies suggest using an object-based image analysis (OBIA) technique to classify UAV imagery and reduce noise by grouping spectrally and spatially similar pixels into features or objects instead of using the raw individual pixels (e.g., Lu et al., 2011; Pérez-Ortiz et al., 2016). There is the potential to reduce noise using OBIA, although additional considerations must be made when generating features such as spectral and spatial detail and scale of segmentation [95] and even then, canopy noise may still be present (e.g., [59])

The most common approach for fractional cover mapping is to use global regression models [96], which assume relationships between dependent and independent variables are spatially homogenous (i.e., constant regression parameters are used over the entire study area). However, as the spectral reflectance signature of vegetation depends on landscape fragmentation, species density, soil quality and age of rehabilitation [86], different plant species are likely to exhibit spectral variability across space [97], which has been shown to make model predictions inaccurate [98]. Our research showed that Geographically Weighted Regression could mitigate these biases by varying the regression coefficients through space [51]. The use of GWR for fractional cover mapping is an emerging area of research [99].

5. Conclusions

Standard UAV imagery cannot reliably discriminate between plant species. However, when aggregated into a dichotomy of weed and native species, overall accuracy exceeds 90%, irrespective of study site. Visible and near infrared bands and their combinations as vegetation indices promote discrimination at this level, as does canopy height, but the red-edge band and textural images were

 doi:10.20944/preprints202312.0441.v1

poor explanatory variables at all our study sites. Fractional cover mapping using GWR improves upon conventional OLS methods and provides a useful way to combine UAV imagery with satellite imagery and summarise the trajectory of native vegetation recovery and potential weed expansion. The combination of UAV imagery with the versatility of dove imagery from cubesats was the most useful approach for gauging recovery and promoting timely intervention to achieve restoration.

Author Contributions: Conceptualisation, T.P.R.; methodology, L.T., and T.P.R.; software, L.T.; validation, A.C. and L.T.; formal analysis, L.T. and T.P.R.; investigation, L.T., T.P.R. and A.C.; resources, T.P.R., L.T. and E.R.; data curation., L.T., T.P.R. and E.R.; writing – original draft preparation, L.T. and T.P.R; writing – review and editing, T.P.R., L.T., A.C. and E.R.; visualisation, L.T.; supervision, T.P.R.; project administration, T.P.R and E.R.; funding acquisition, T.P.R. and E.R. All authors have read and agreed to the published version of the manuscript.

Funding: This research was funded by the Water Corporation of Western Australia.

Data Availability Statement: For data accessibility please contact the corresponding author.

Acknowledgments: This study acknowledges the Water Corporation of Western Australia for funding the research. The authors would like to thank Zoe Webber from Curtin University for her support validating plant samples.

Conflicts of Interest: The authors declare no conflict of interest. The funds have had no role in the design of the study; in the collection, analyses, or interpretation of data; in the writing of the manuscript; or in the decision to publish results.

Appendix A. Species inventories

Table A1. Species inventory observed at the Lancelin study site.

Species or Land-use/cover Class	Type	Included	Num. ROIs	Num. Pixels
Acacia cyclops	Native	Yes	25	2500
Acacia cyclops (Dead)	Native	No	-	-
Acacia xanthina	Native	No	-	-
Acanthocarpus preissii	Native	Yes	32	3200
Acrotriche cordata	Native	No	-	-
Agonis flexuosa	Native	Yes	22	2200
Allocasuarina lehmanniana (darker)	Native	Yes	21	2100
Allocasuarina lehmanniana (lighter)	Native	Yes	30	3000
Austrostipa elegantissima	Native	Yes	24	2400
Eucalyptus sp.	Native	No	-	-
Eucalyptus sp. decipiens?	Native	No	-	-
Ficinia nodosa	Native	No	-	-
Lepidosperma gladiatum	Native	Yes	26	2600
Macrozamia sp.	Native	No	-	-
Melaleuca cardiophylla	Native	Yes	35	3500
Melaleuca lanceolata	Native	No	-	-
Myoporum insulare	Native	Yes	31	3100
Myrtaceae sp.	Native	No	-	-
Olearia axillaris	Native	Yes	24	2400
Red Moss sp.	Native	Yes	28	2800
Scaevola crassifolia	Native	Yes	27	2700
Schoenus caespititius	Native	No	-	-
Spyridium globulosum	Native	Yes	20	2000
Tersonia cyathiflora	Native	No	-	-
**Cenchrus ciliaris*[1]	Exotic	Yes	33	3300
**Ehrharta villosa*	Exotic	Yes	35	3500
**Galium* sp.[1]	Exotic	Yes	27	2700
**Gazania linearis*[1]	Exotic	Yes	31	3100
**Gomphocarpus fruticosus*	Exotic	Yes	24	2400

Preprints (www.preprints.org) | NOT PEER-REVIEWED | Posted: 7 December 2023 doi:10.20944/preprints202312.0441.v1

**Hypochaeris glabra*[1]	Exotic	Yes	28	2800
**Oxalis pes-caprae*[1]	Exotic	Yes	32	3200
**Pelargonium capitatum*	Exotic	No	-	-
**Poa annua*[1]	Exotic	Yes	23	2300
Dead Grass (Light Brown)	Other	Yes	28	2800
Dead Material	Other	Yes	25	2500
Exposed Dead Grass (White)	Other	Yes	23	2300
Exposed Dead Grass and Soil (Grey)	Other	Yes	27	2700
Sand (White)	Other	Yes	20	2000
Sand (Yellow)	Other	Yes	21	2100

[1] Grouped into a * Lawn Weeds class as all species were observed growing heavily mixed together.

Table A2. Species inventory observed at the City Beach study site.

Species or Land-use/cover Class	Type	Included	Num. ROIs	Num. Pixels
Acacia cyclops	Native	Yes	45	4500
Acacia lasiocarpa	Native	Yes	47	4700
Acacia rostellifera	Native	Yes	47	4700
Acacia sp. whispy leaves	Native	No	-	-
Acanthocarpus preissii	Native	Yes	49	4900
Allocasuarina lehmanniana	Native	Yes	39	3900
Austrostipa elegantissisma	Native	Yes	43	4300
Calothamnus quadrifidus	Native	Yes	40	4000
Carpobrotus virescens	Native	No	-	-
Conostylis candicans	Native	No	-	-
Eucalyptus sp. huge leaves	Native	Yes	39	3900
Ficinia nodosa	Native	Yes	46	4600
Grevillea preissii	Native	Yes	44	4400
Hardenbergia comptoniana	Native	No	-	-
Lepidosperma gladiatum	Native	Yes	48	4800
Melaleuca cardiophylla	Native	Yes	40	4000
Melaleuca lanceolata	Native	Yes	47	4700
Melaleuca sp. dark leaves	Native	No	-	-
Melaleuca sp. extra small leaves	Native	No	-	-
Melaleuca huegelii subsp. *huegelii*	Native	Yes	43	4300
Melaleuca systena	Native	No	-	-
Olearia axillaris	Native	Yes	47	4700
Rhagodia baccata	Native	Yes	43	4300
Santalum acuminatum	Native	No	-	-
Scaevola crassifolia	Native	Yes	45	4500
Spinifex longifolia	Native	Yes	44	4400
Spyridium globulosum	Native	Yes	38	3800
Templetonia retusa	Native	Yes	39	3900
Tersonia cyathiflora	Native	No	-	-
**Ehrharta calycina*	Exotic	No	-	-
**Lagurus ovatus*	Exotic	No	-	-
**Pelargonium capitatum*	Exotic	Yes	44	4400
**Urospermum picroides*	Exotic	No	-	-
Dead branches	Other	Yes	42	4200
Path (brown)	Other	Yes	46	4600
Path (white)	Other	Yes	42	4200
Road	Other	Yes	40	4000
Sand (white)	Other	Yes	39	3900

Preprints (www.preprints.org) | NOT PEER-REVIEWED | Posted: 7 December 2023 doi:10.20944/preprints202312.0441.v1

Sand (yellow)	Other	Yes	47	4700
Woodchips	Other	Yes	39	3900

Table A3. Species inventory observed at the Goegrup study site.

Species or Land-use/cover Class	Type	Included	Num. ROIs	Num. Pixels
Allocasuarina fraseriana	Native	Yes	46	4600
Agonis flexuosa	Native	Yes	41	4100
Banksia menziesii	Native	No	-	-
Carpobrotus virescens	Native	No	-	-
Corymbia calophylla	Native	Yes	42	4200
Eucalyptus gomphocephala	Native	Yes	41	4100
Eucalyptus rudis	Native	Yes	38	3800
Exocarpus sparteus	Native	No	-	-
Gahnia trifida	Native	Yes	39	3900
Grevillea vestita	Native	No	-	-
Hardenbergia comptoniana	Native	Yes	46	4600
Jacksonia furcellata	Native	Yes	39	3900
Juncus kraussii	Native	Yes	39	3900
Lomandra caespitosa	Native	Yes	43	4300
Machaerina juncea	Native	Yes	41	4100
Macrozamia fraseri	Native	Yes	38	3800
Melaleuca rhaphiophylla	Native	Yes	43	4300
Regelia ciliata	Native	Yes	41	4100
Tecticornia pergranulata	Native	Yes	40	4000
**Arctotheca calendula*	Exotic	Yes	40	4000
**Atriplex prostrata*	Exotic	No	-	-
**Avena barbata*	Exotic	Yes	44	4400
**Briza maxima*	Exotic	Yes	44	4400
**Cynodon dactylon*	Exotic	Yes	42	4200
**Lagurus ovatus*	Exotic	Yes	45	4500
**Lupinus cosentinii*	Exotic	No	-	-
**Oenothera stricta*	Exotic	No	-	-
**Pelargonium capitatum*	Exotic	No	-	-
Dead branches	Other	Yes	47	4700
Dead Grass Weeds	Other	Yes	46	4600
Metal	Other	Yes	41	4100
Path (brown)	Other	Yes	38	3800
Path (red)	Other	Yes	41	4100
Road	Other	Yes	38	3800
Sand (light brown)	Other	Yes	42	4200
Sand (white)	Other	Yes	40	4000
Sand (yellow)	Other	Yes	42	4200
Shadows	Other	Yes	47	4700
Water	Other	Yes	42	4200
Water (swamp)	Other	Yes	43	4300

Preprints (www.preprints.org) | NOT PEER-REVIEWED | Posted: 7 December 2023 doi:10.20944/preprints202312.0441.v1

Appendix B Confusion matrices calculated with user and producer error for broad- and species-level training data at Lancelin, City Beach and Goegrup study sites

Table A4. Confusion matrix calculated with user and producer error using species-level training data for Lancelin study site.

	Myo. ins.	*Aca. cyc.*	*Lep. gla.*	*Ole. axi.*	*Spy. glo.*	*Ago. fle.*	*Mel. car.*	*Sca. cra.*	**Ehr. vil.*	**Gom. fru.*	*Red Moss*	*Aca. pre.*	*Aus. ele.*	*All. leh. (dark)*	*All. leh. (light)*	**Lawn Weeds*	Other	User's Accuracy (%)
Myo. ins.	72	3	1	0	19	10	17	9	2	8	0	8	1	4	15	5	0	41.4
Aca. cyc.	6	102	0	0	1	2	0	1	0	0	0	0	0	0	2	0	0	89.5
Lep. gla.	1	0	101	0	0	0	0	0	9	0	0	3	0	10	0	0	0	81.5
Ole. axi.	0	0	0	111	0	0	0	1	2	1	0	0	0	1	0	0	0	95.7
Spy. glo.	9	1	0	0	73	6	3	3	0	2	0	8	3	0	1	0	0	67.0
Ago. fle.	4	0	0	0	8	80	5	7	7	1	0	0	0	0	0	1	0	70.8
Mel. car.	12	0	0	0	4	7	89	5	1	5	0	8	0	0	1	0	0	67.4
Sca. cra.	3	3	1	0	4	3	0	83	5	1	0	1	0	0	4	1	0	76.1
**Ehr. vil.*	0	0	2	0	1	2	0	3	81	0	0	4	0	0	0	0	0	87.1
**Gom. fru.*	3	0	0	3	0	1	0	0	0	69	0	0	10	0	0	27	0	61.1
Red Moss	0	0	0	1	0	0	0	0	0	1	117	0	0	0	0	1	5	93.6
Aca. pre.	0	2	4	1	1	2	0	0	5	0	0	71	22	0	13	3	1	56.8
Aus. ele.	0	0	0	0	3	1	2	0	0	1	0	9	74	0	1	1	0	80.4
All. leh. (dark)	0	4	5	0	0	0	0	1	0	0	0	0	0	87	10	0	0	81.3
All. leh. (light)	5	2	3	0	2	1	1	2	0	0	0	4	0	15	69	1	0	65.7
*Lawn Weeds	2	0	0	1	1	2	0	2	5	27	0	0	7	0	1	76	0	61.3
Other	0	0	0	0	0	0	0	0	0	1	0	1	0	0	0	1	111	97.4
Prod. Accuracy (%)	61.5	87.2	86.3	94.9	62.4	68.4	76.1	70.9	69.2	59.0	100.0	60.7	63.2	74.4	59.0	65.0	94.9	73.7
Overall Accuracy	73.7																	
Kappa	0.72																	

 doi:10.20944/preprints202312.0441.v1

Table A5. Confusion matrix calculated with user and producer error using broad-level training data for Lancelin study site.

	Other	Native	Exotic	User's Accuracy (%)
Other	653	9	27	94.8
Native	7	612	52	91.2
Exotic	6	45	587	92.0
Prod. Accuracy (%)	98.0	91.9	88.1	
Overall Accuracy (%)	98.1			
Kappa	0.90			

 doi:10.20944/preprints202312.0441.v1

Table A6. Confusion matrix calculated with user and producer error using species-level training data for City Beach study site.

	Ole. axi.	*Sca. cra.*	*Spi. lon.*	*Fic. nod.*	*Aus. ele.*	*Aca. ros.*	*Aca. cyc.*	**Pel. cap.*	*Spy. glo.*	*Rha. bac.*	*All. leh.*	*Lep. gla.*	*Aca. las.*	*Cal. qua.*	*Mel. hue.*	*Mel. car.*	*Mel. lan.*	*Euc.* sp.	*Aca. pre.*	*Tem. ret.*	*Gre. pre.*	Other	User's Accuracy (%)
Ole. axi.	87	0	3	0	0	0	0	0	0	1	0	0	0	0	0	0	0	0	2	0	0	0	93.6
Sca. cra.	0	68	0	1	0	3	0	0	0	0	0	6	4	2	0	0	2	0	0	1	0	0	78.2
Spi. lon.	0	0	64	0	6	0	0	0	0	0	0	0	0	0	0	0	0	0	5	0	0	0	85.3
Fic. nod.	0	13	3	80	1	0	0	13	0	0	0	5	0	0	0	0	0	0	2	0	0	1	67.8
Aus. ele.	0	0	13	1	78	0	0	0	0	3	0	3	0	0	0	0	0	0	1	0	0	0	78.8
Aca. ros.	0	0	0	0	0	53	6	0	3	0	1	0	0	1	0	1	0	2	0	7	0	0	71.6
Aca. cyc.	0	0	0	0	0	17	66	0	1	0	6	0	0	0	0	0	0	0	0	0	0	0	73.3
**Pel. cap.*	0	0	0	6	0	0	0	75	0	0	0	0	0	0	0	0	0	0	0	0	0	0	92.6
Spy. glo.	0	0	0	0	0	0	2	0	41	0	2	0	2	12	6	6	2	0	0	7	7	0	47.1
Rha. bac.	2	3	0	0	1	5	3	0	0	72	0	5	4	6	3	0	0	0	0	11	0	0	62.6
All. leh.	0	0	0	0	0	0	4	0	4	0	57	0	0	5	7	1	1	0	0	2	1	0	69.5
Lep. gla.	0	5	0	1	1	2	0	1	0	10	0	67	3	0	3	0	0	0	4	0	1	0	68.4
Aca. las.	0	1	0	0	0	0	0	0	0	1	0	0	58	9	0	0	1	0	0	4	2	0	76.3
Cal. qua.	0	0	0	0	0	0	0	0	9	0	2	0	7	46	0	0	9	0	0	3	17	0	49.5
Mel. hue.	1	0	0	0	0	0	3	0	4	1	4	2	0	0	55	6	0	0	2	0	2	0	68.8
Mel. car.	0	0	0	0	0	0	3	0	6	0	7	0	0	1	10	57	3	0	0	3	1	0	62.6
Mel. lan.	0	0	0	0	0	3	0	0	3	0	3	0	0	2	2	14	71	0	0	4	3	0	67.6
Euc. sp.	0	0	0	0	0	5	0	0	0	0	0	0	0	0	0	0	0	88	0	0	0	0	94.6
Aca. pre.	0	0	7	1	3	0	0	1	0	1	0	0	0	0	0	0	0	0	74	0	0	0	85.1
Tem. ret.	0	0	0	0	0	1	3	0	6	1	1	0	0	1	0	1	1	0	0	40	1	0	71.4
Gre. pre.	0	0	0	0	0	1	0	0	13	0	7	2	12	5	4	4	0	0	0	8	55	0	49.6
Other	0	0	0	0	0	0	0	0	0	0	0	0	0	0	0	0	0	0	0	0	0	89	100.0
Prod. Accuracy (%)	96.7	75.6	71.1	88.9	86.7	58.9	73.3	83.3	45.6	80.0	63.3	74.4	64.4	51.1	61.1	63.3	78.9	97.8	82.2	44.4	61.1	98.9	
Overall Accuracy (%)	72.8																						
Kappa	0.71																						

 doi:10.20944/preprints202312.0441.v1

Table A7. Confusion matrix calculated with user and producer error using broad-level training data for City Beach study site.

	Other	Native	Exotic	User's Accuracy (%)
Other	664	18	5	96.65
Native	0	631	25	96.19
Exotic	2	17	636	97.1
Prod. Accuracy (%)	99.7	94.74	95.5	
Overall Accuracy (%)	96.6			
Kappa	0.95			

 doi:10.20944/preprints202312.0441.v1

Table A8. Confusion matrix calculated with user and producer error using species-level training data for Goegrup study site.

	All. fra.	*Euc. gom.*	*Euc. rud.*	*Mac. jun.*	*Jac. fur.*	*Reg. cil.*	*Mel. rha.*	*Har. com.*	*Tec. per.*	*Mac. fra.*	*Jun. kra.*	*Cor. cal.*	*Lom.* cae.	*Ago. fle.*	*Gah. tri.*	**Lag. ova.*	**Ave bar.*	**Cyn. dac.*	**Arc.* cal.	**Bri. max.*	Other	User's Accuracy (%)
All. fra.	88	0	1	0	0	0	2	0	0	0	0	3	0	3	2	0	0	0	0	0	0	88.9
Euc. gom.	0	78	9	0	0	0	0	0	0	0	0	2	0	1	0	0	0	0	0	0	0	86.7
Euc. rud.	3	12	83	0	0	0	0	0	0	0	0	6	0	6	0	0	0	0	0	0	0	75.5
Mac. jun.	0	0	0	62	0	4	0	0	2	0	0	0	5	0	2	1	6	6	2	2	0	67.4
Jac. fur.	0	1	0	0	65	0	18	0	0	0	0	0	0	0	0	0	0	0	0	0	0	77.4
Reg. cil.	0	1	0	3	4	68	2	0	1	1	1	2	6	0	2	0	0	0	0	0	0	74.7
Mel. rha.	4	0	1	0	17	0	73	0	0	0	0	0	0	0	0	0	0	0	0	0	0	76.8
Har. com.	0	0	0	0	0	0	0	84	0	0	0	0	0	0	4	0	0	0	0	1	0	94.4
Tec. per.	0	0	0	0	0	2	0	0	91	0	2	0	4	0	2	4	4	0	0	0	3	81.3
Mac. fra.	0	1	0	0	0	4	0	4	0	81	17	0	0	0	3	0	0	0	0	0	0	73.6
Jun. kra.	0	2	0	0	2	2	0	0	0	4	62	0	0	0	1	0	0	0	0	0	3	81.6
Cor. cal.	0	0	1	0	0	0	0	0	0	0	0	81	0	0	1	0	0	0	0	0	0	97.6
Lom. cae.	0	0	0	23	6	6	0	0	1	2	6	0	66	0	0	1	6	0	5	0	1	53.7
Ago. fle.	0	0	0	0	1	0	0	0	0	0	0	0	0	85	1	0	0	0	0	0	0	97.7
Gah. tri.	0	0	0	1	0	9	0	5	0	4	2	0	0	0	77	0	0	0	4	0	0	75.5
**Lag. ova.*	0	0	0	1	0	0	0	0	0	2	0	0	1	0	0	40	21	5	3	0	0	54.8
**Ave bar.*	0	0	0	2	0	0	0	0	0	1	0	1	10	0	0	31	29	3	7	0	3	33.3
**Cyn. dac.*	0	0	0	0	0	0	0	1	0	0	0	0	0	0	0	1	9	67	13	5	0	69.8
**Arc. cal.*	0	0	0	3	0	0	0	0	0	0	0	0	3	0	0	13	17	8	59	0	0	57.3
**Bri. max.*	0	0	0	0	0	0	0	1	0	0	0	0	0	0	0	0	2	6	2	87	0	88.8
Other	0	0	0	0	0	0	0	0	0	0	5	0	0	0	0	4	1	0	0	0	85	89.5
Prod. Accuracy (%)	92.6	82.1	87.4	65.3	68.4	71.6	76.8	88.4	95.8	85.3	65.3	85.3	69.5	89.5	81.1	42.1	30.5	70.5	62.1	91.6	89.5	
Overall Accuracy (%)	75.7																					
Kappa	0.75																					

Preprints (www.preprints.org) | NOT PEER-REVIEWED | Posted: 7 December 2023 doi:10.20944/preprints202312.0441.v1

Table A9. Confusion matrix calculated with user and producer error using broad-level training data for Goegrup study site.

	Other	Native	Exotic	User's Accuracy (%)
Other	647	26	6	95.3
Native	12	599	41	91.9
Exotic	7	41	619	92.8
Prod. Accuracy (%)	97.1	89.9	92.9	
Overall Accuracy (%)	93.3			
Kappa	0.91			

Appendix C. Random Forest classification results for broad- and species-level training data at Lancelin, City Beach and Goegrup study sites

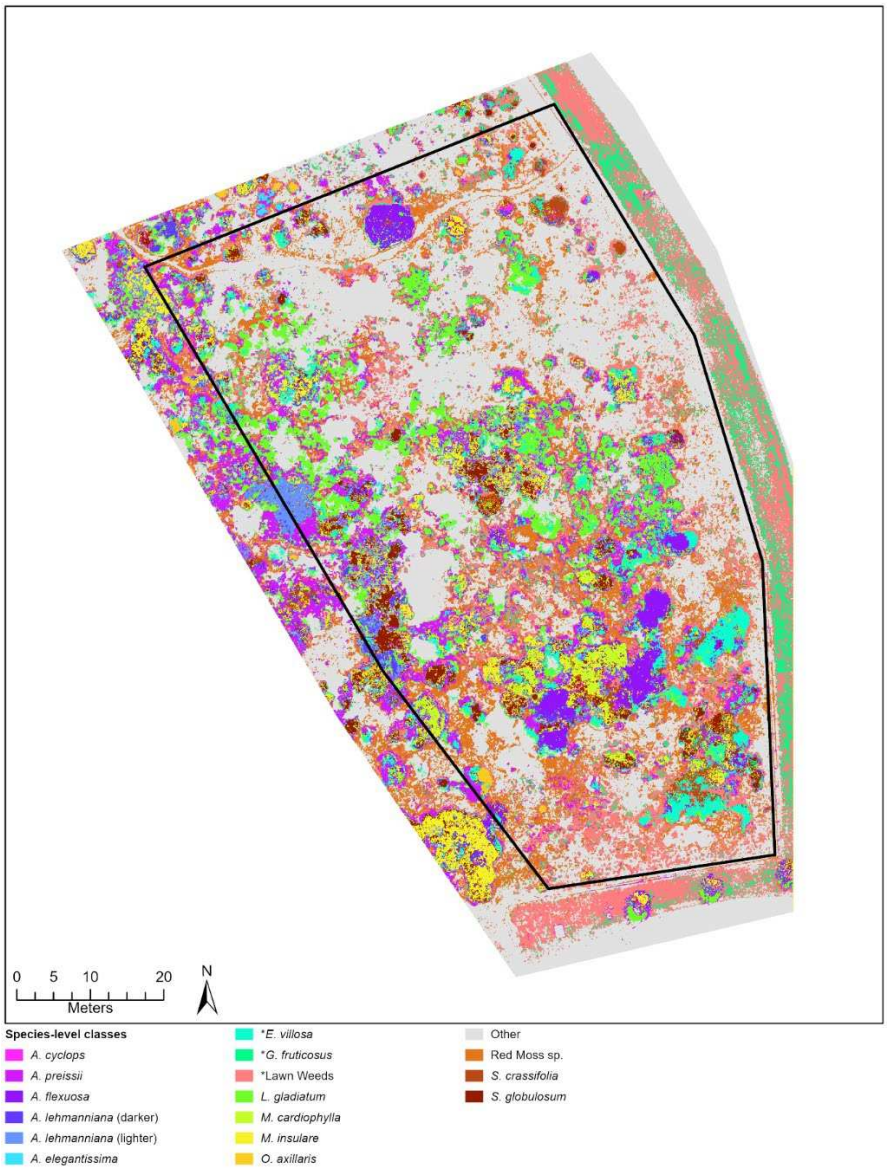

Figure A1. Random Forest classification results for species-level training data for Lancelin study site.

Preprints (www.preprints.org) | NOT PEER-REVIEWED | Posted: 7 December 2023 doi:10.20944/preprints202312.0441.v1

.

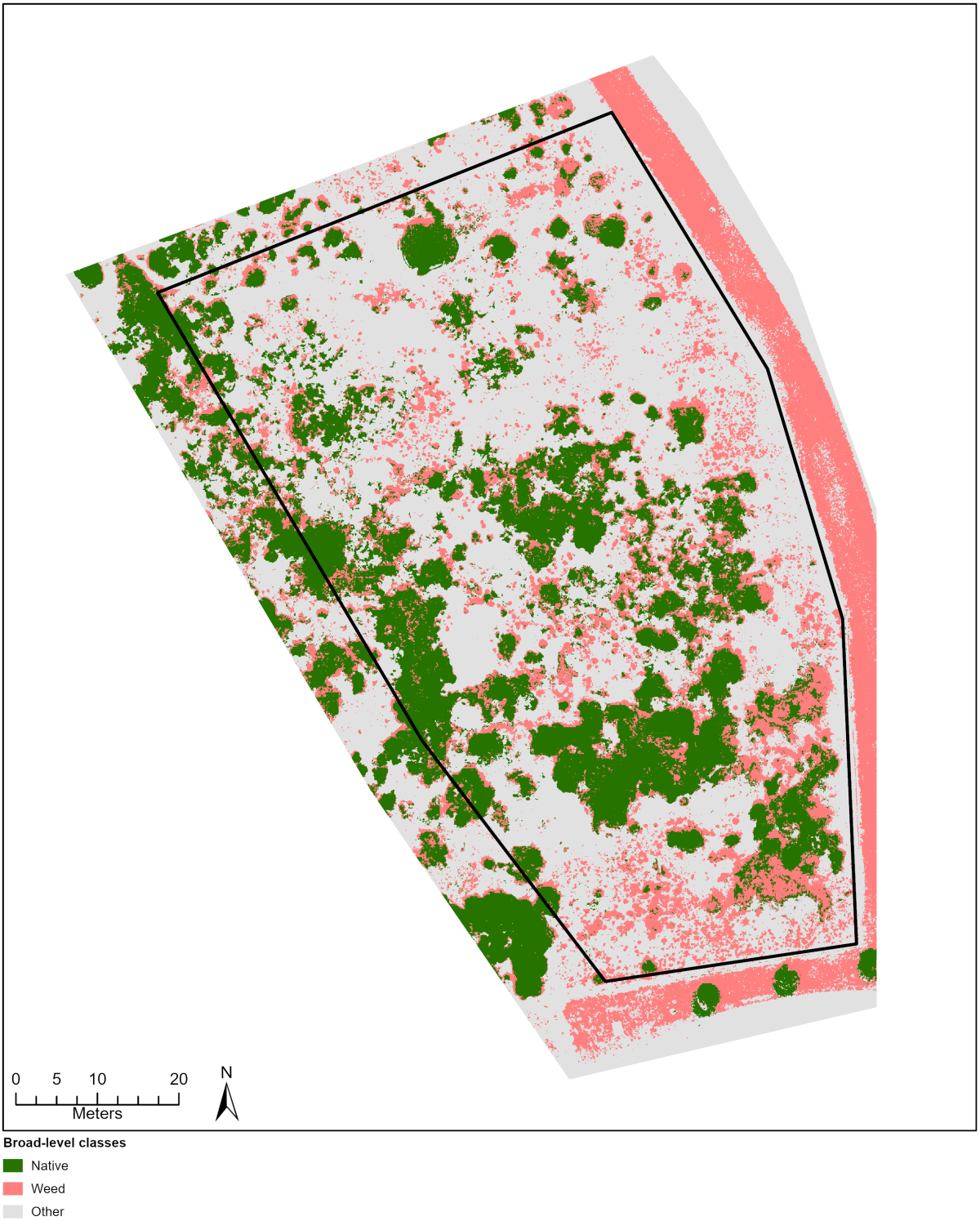

Figure A2. Random Forest classification results for broad-level training data for Lancelin study site.

Preprints (www.preprints.org) | NOT PEER-REVIEWED | Posted: 7 December 2023 doi:10.20944/preprints202312.0441.v1

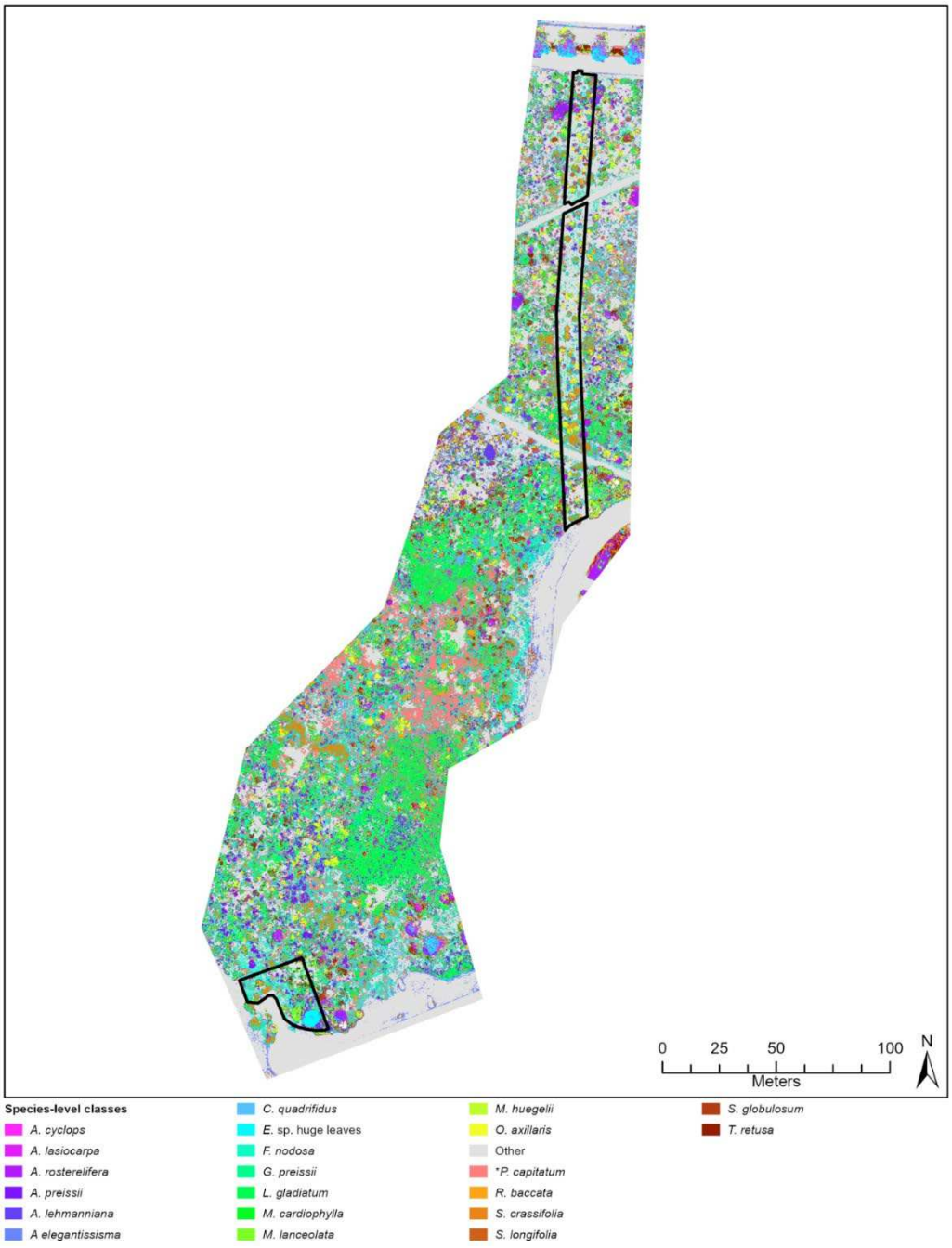

Figure A3. Random Forest classification results for species-level training data for City Beach study site.

Preprints (www.preprints.org) | NOT PEER-REVIEWED | Posted: 7 December 2023 doi:10.20944/preprints202312.0441.v1

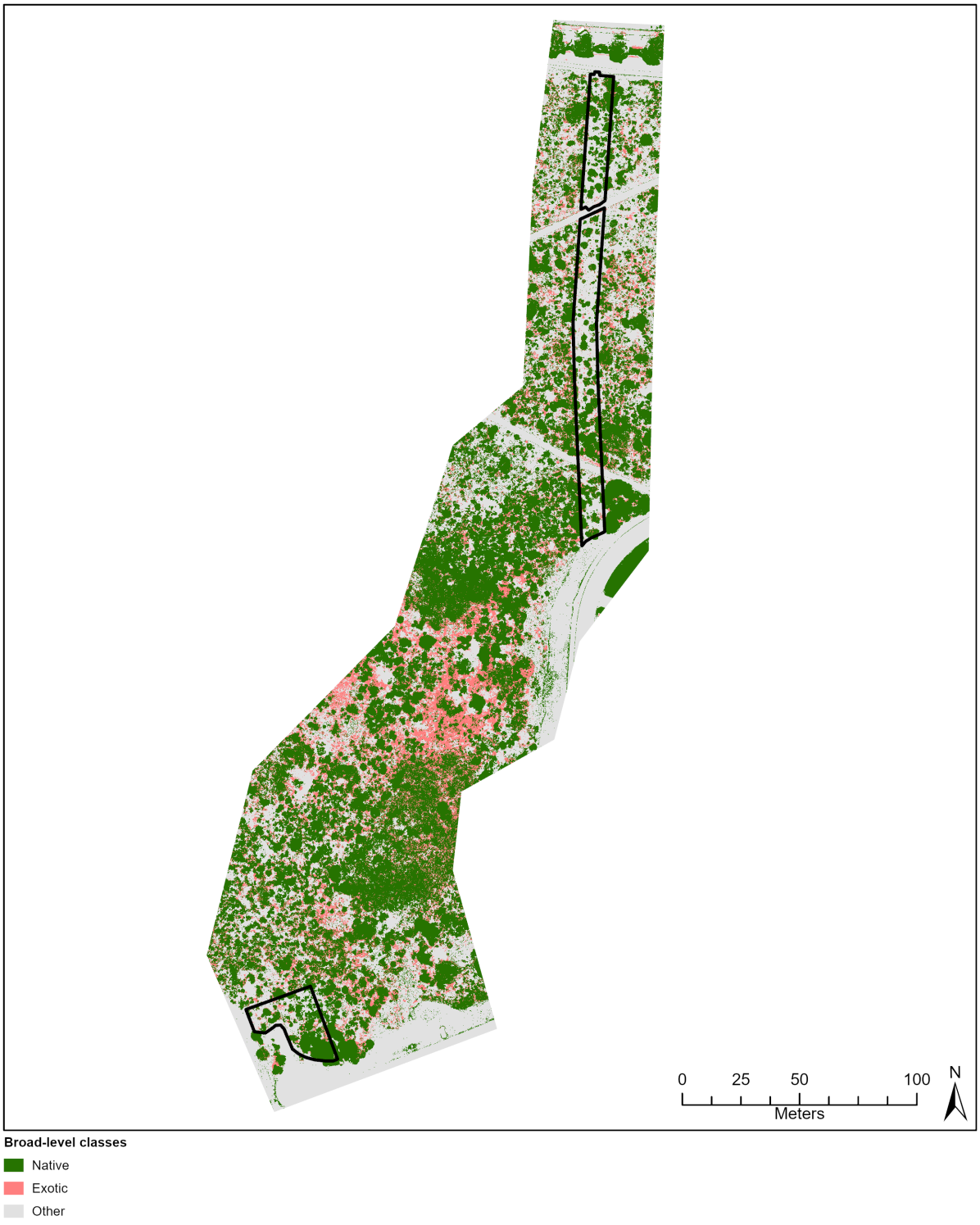

Figure A4. Random Forest classification results for broad-level training data for City Beach study site.

Preprints (www.preprints.org) | NOT PEER-REVIEWED | Posted: 7 December 2023 doi:10.20944/preprints202312.0441.v1

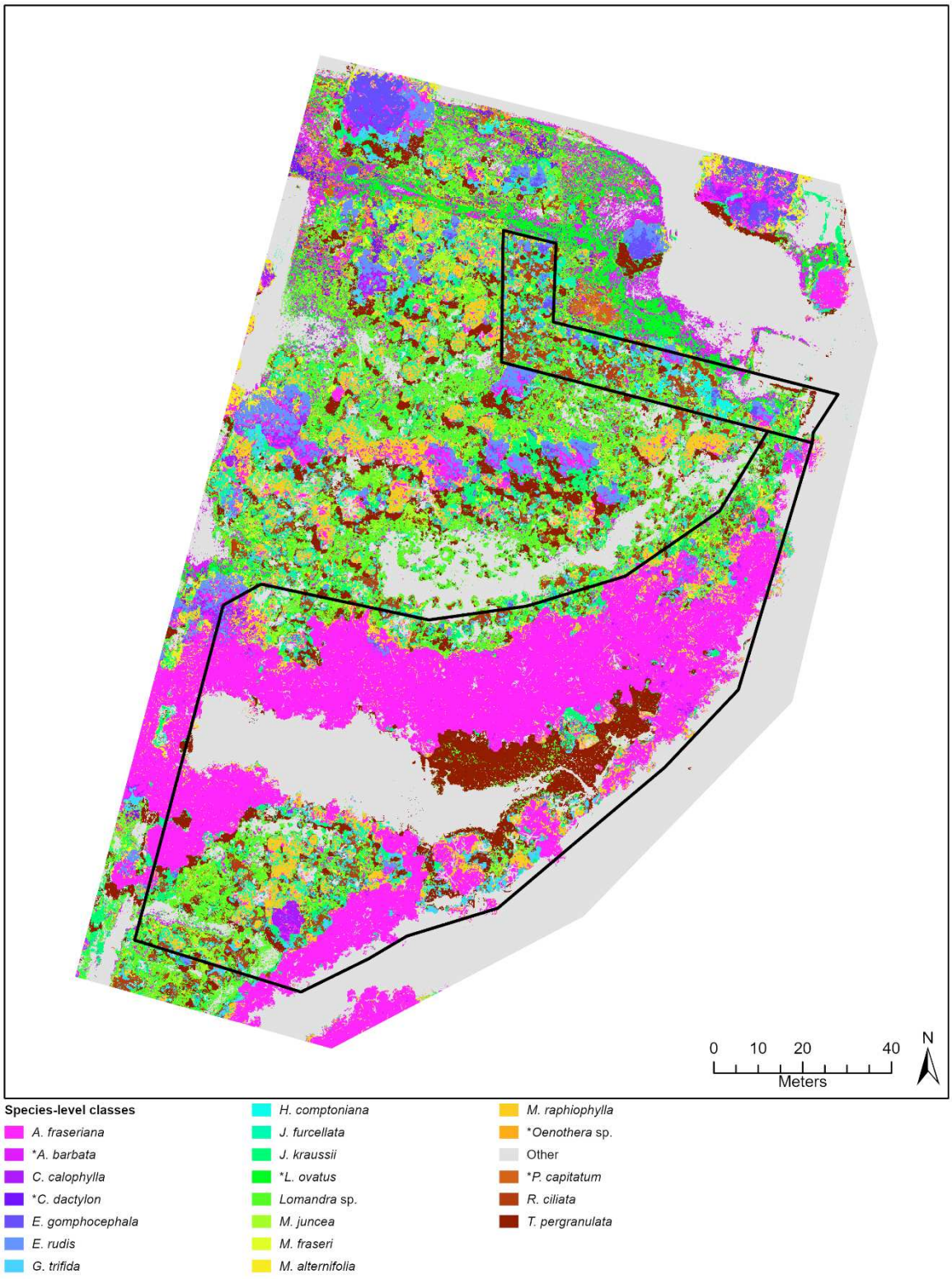

Figure A5. Random Forest classification results for species-level training data for Goegrup study site.

Preprints (www.preprints.org) | NOT PEER-REVIEWED | Posted: 7 December 2023 doi:10.20944/preprints202312.0441.v1

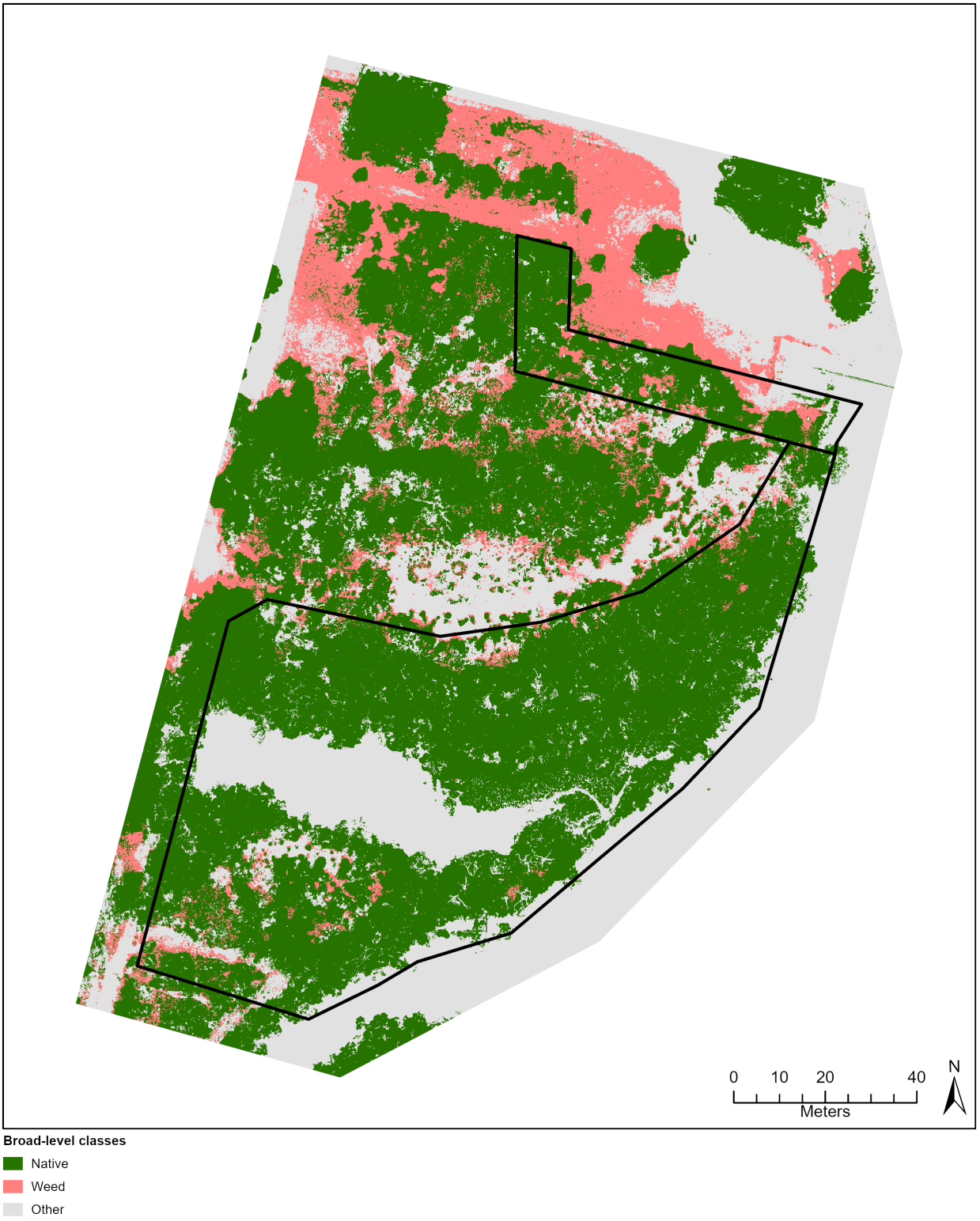

Figure A6. Random Forest classification results for broad-level training data for Goegrup study site.

 doi:10.20944/preprints202312.0441.v1

Appendix D. Akaike information criterion (AIC) value produced from the fractional cover modelling procedure based on Ordinary Least Squares (OLS) and Geographically-Weighted Regression (GWR) techniques.

Table A10. Akaike information criterion (AIC) value produced from the fractional cover modelling procedure based on Ordinary Least Squares (OLS) and Geographically-Weighted Regression (GWR) techniques. Both methods were applied to Sentinel-2 and PlanetScope images over the period 2015 to 2023 at Lancelin, City Beach and Goegrup study sites.

		Lancelin Site				**City Beach Site**				**Goegrup Site**			
		Sentinel-2		**Planet**		**Sentinel-2**		**Planet**		**Sentinel-2**		**Planet**	
	Year	**OLS**	**GWR**	**OLS**	**GWR**	**OLS**	**GWR**	**OLS**	**GWR**	**OLS**	**GWR**	**OLS**	**GWR**
Natives Fractions	2015	-172	-190	-	-	-	-	-	-	-79	-182	-	-
	2016	-166	-179	-155	-804	-469	-594	-	-	-45	-149	-1596	-3424
	2017	-166	-185	-126	-735	-375	-588	-710	-2742	-43	-126	-2042	-2678
	2018	-148	-177	-259	-784	-402	-589	-910	-2808	-16	-226	-2026	-2885
	2019	-173	-205	-222	-941	-404	-566	-182	-3840	-26	-155	-2025	-2795
	2020	-158	-182	-289	-1229	-430	-587	-560	-4314	-14	-152	-1578	-2334
	2021	-183	-222	-409	-1180	-434	-609	-294	-3658	-71	-161	-1767	-3402
	2022	-196	-225	-438	-1161	-581	-697	-811	-4849	-88	-219	-2056	-2771
	2023	-	-	-	-	-634	-742	-751	-3386	-	-	-	-
	Mean	-170	-196	-271	-976	-442	-604	-578	-3702	-48	-171	-1870	-2898
Exotic Fractions	2015	-193	-225	-	-	-	-	-	-	-468	-616	-	-
	2016	-185	-209	-959	-2174	-1723	-2092	-	-	-501	-608	-2337	-5694
	2017	-208	-235	-968	-1914	-1746	-2127	-1320	-1853	-487	-560	-1917	-5813
	2018	-180	-217	-929	-1843	-1793	-2157	-1285	-1874	-510	-593	-2065	-5694
	2019	-202	-221	-1057	-2159	-1768	-2159	-1312	-1888	-506	-591	-1902	-5627
	2020	-217	-226	-1267	-2276	-1816	-2146	-1292	-1896	-510	-649	-2204	-6157
	2021	-187	-218	-1062	-2198	-1764	-2161	-1298	-1850	-520	-644	-2472	-6233
	2022	-173	-212	-978	-2103	-1827	-2208	-1288	-1918	-529	-665	-1812	-6212
	2023	-	-	-	-	-1844	-2209	-1293	-1851	-	-	-	-
	Mean	-193	-220	-1032	-2095	-1777	-2150	-1299	-1880	-504	-616	-2101	-5919

Preprints (www.preprints.org) | NOT PEER-REVIEWED | Posted: 7 December 2023 doi:10.20944/preprints202312.0441.v1

Appendix E. Three band RGB (red, green, blue) trend rasters depicting rehabilitation condition change at anniverisary dates over multiple years at Lancelin and Goegrup Reserve sites.

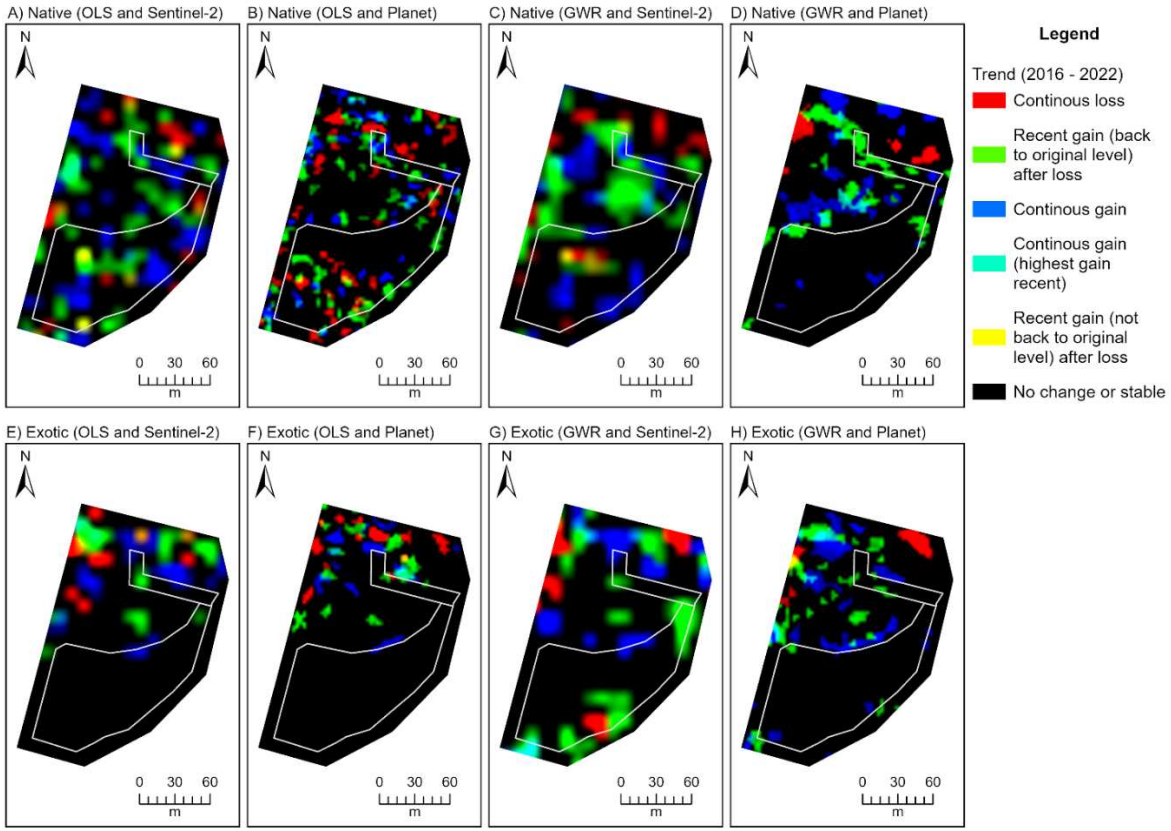

Figure A7. Three band RGB (red, green, blue) trend rasters depicting rehabilitation condition change every November over the period 2016 to 2022 at the Goegrup Reserve site. Trends are derived from temporal fractional models representing natives (A-D) and exotics (E-H). Trend rasters produced from the Sentinel-2 (A, C, E, G) and Planet (B, D, F, H) fraction models and ordinary least squares (OLS; A, B, E, F) and geographically weighted regression (GWR; C, D, G, H) techniques are provided.

Preprints (www.preprints.org) | NOT PEER-REVIEWED | Posted: 7 December 2023 doi:10.20944/preprints202312.0441.v1

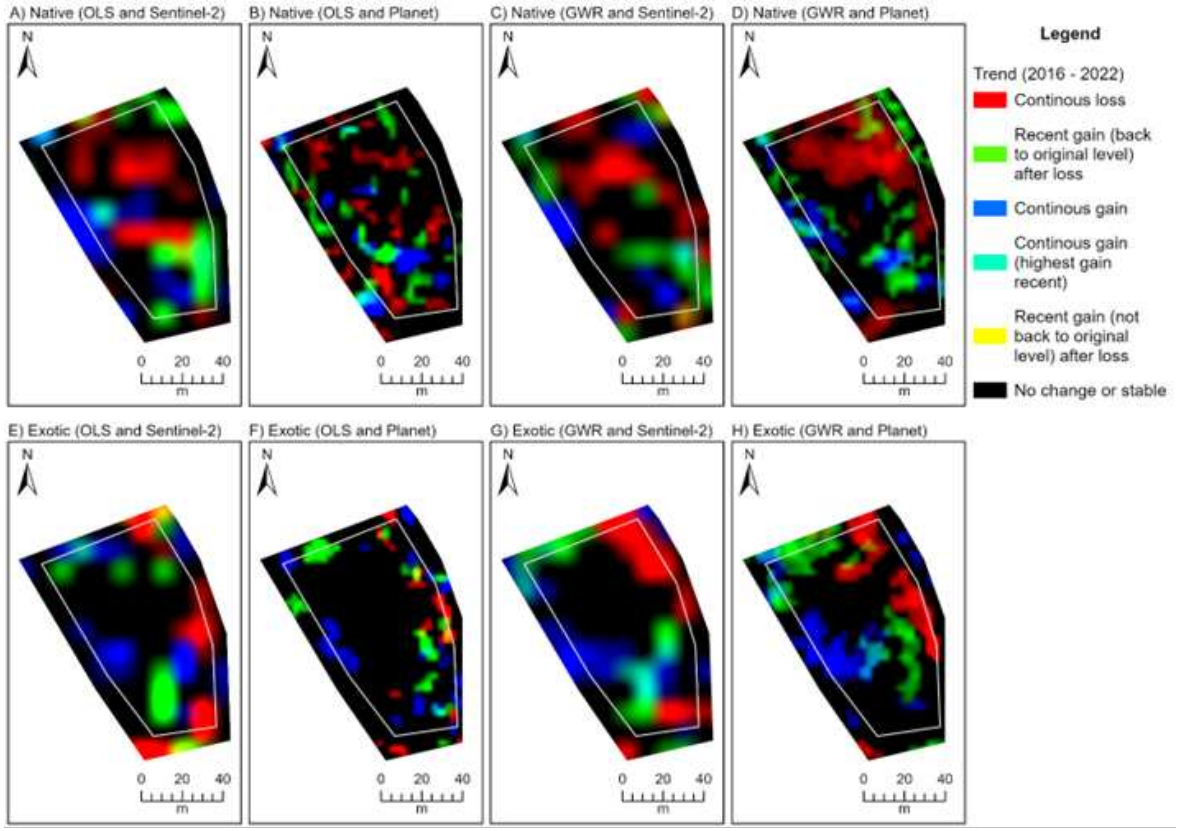

Figure A8. Three band RGB (red, green, blue) trend rasters depicting rehabilitation condition change every November over the period 2016 to 2022 at the Lancelin site. Trends are derived from temporal fractional models representing natives (A-D) and exotics (E-H). Trend rasters produced from the Sentinel-2 (A, C, E, G) and Planet (B, D, F, H) fraction models and ordinary least squares (OLS; A, B, E, F) and geographically weighted regression (GWR; C, D, G, H) techniques are provided. .

References

1. Ruiz-Jaen, M.C. and Mitchell Aide, T., 2005. Restoration success: how is it being measured?. Restoration Ecology, 13(3), pp.569-577.
2. Benayas, J.M.R., Newton, A.C., Diaz, A. and Bullock, J.M., 2009. Enhancement of biodiversity and ecosystem services by ecological restoration: a meta-analysis. science, 325(5944), pp.1121-1124.
3. Possingham, H.P., Bode, M. and Klein, C.J., 2015. Optimal conservation outcomes require both restoration and protection. PLoS biology, 13(1), p.e1002052.
4. Herrick, J.E., Schuman, G.E. and Rango, A., 2006. Monitoring ecological processes for restoration projects. Journal for Nature Conservation, 14(3-4), pp.161-171.
5. Anderson, K. and Gaston, K.J. (2013) 'Lightweight unmanned aerial vehicles will revolutionize spatial ecology', Frontiers in Ecology and the Environment, 11(3), pp. 138–146. doi:10.1890/120150.
6. Buters, T.M., Bateman, P.W., Robinson, T., Belton, D., Dixon, K.W. and Cross, A.T., 2019. Methodological ambiguity and inconsistency constrain unmanned aerial vehicles as a silver bullet for monitoring ecological restoration. Remote Sensing, 11(10), p.1180.
7. Rose, M.B., Mills, M., Franklin, J. and Larios, L., 2023. Mapping Fractional Vegetation Cover Using Unoccupied Aerial Vehicle Imagery to Guide Conservation of a Rare Riparian Shrub Ecosystem in Southern California. Remote Sensing, 15(21), p.5113.
8. Loarie, S.R., Joppa, L.N. and Pimm, S.L., 2007. Satellites miss environmental priorities. Trends in Ecology & Evolution, 22(12), pp.630-632.
9. Gómez-Sapiens, M., Schlatter, K.J., Meléndez, Á., Hernández-López, D., Salazar, H., Kendy, E. and Flessa, K.W., 2021. Improving the efficiency and accuracy of evaluating aridland riparian habitat restoration using unmanned aerial vehicles. Remote Sensing in Ecology and Conservation, 7(3), pp.488-503.
10. Huang, C.Y. and Asner, G.P., 2009. Applications of remote sensing to alien invasive plant studies. Sensors, 9(6), pp.4869-4889.
11. Planetscope (2023). Available at: https://developers.planet.com/docs/data/planetscope/ (Accessed: 03 November 2023).
12. McKenna, P.B., Lechner, A.M., Hernandez Santin, L., Phinn, S. and Erskine, P.D., 2023. Measuring and monitoring restored ecosystems: can remote sensing be applied to the ecological recovery wheel to inform restoration success? Restoration Ecology, 31(1), p.e13724.
13. MicaSense, 2021. RedEdge-P Integration Guide. Available at: https://support.micasense.com/hc/en-us/articles/4410824602903-RedEdge-P-Integration-Guide [Accessed on 1 March 2023].
14. DJI, 2023. Zenmuse P1 Specifications. Available at: https://enterprise.dji.com/zenmuse-p1/specs (Accessed:1 March 2023).
15. Pix4D, 2023. Available online: www.pix4d.com (accessed on 1 March 2023).
16. Ruwaimana, M., Satyanarayana, B., Otero, V., M. Muslim, A., Syafiq A, M., Ibrahim, S., Raymaekers, D., Koedam, N. and Dahdouh-Guebas, F., 2018. The advantages of using drones over space-borne imagery in the mapping of mangrove forests. PloS one, 13(7), p.e0200288.
17. Digital Earth Australia. 2023. Available at: https:// https://www.dea.ga.gov.au/ (Accessed: 15 August 2023).
18. Farmonov, N., Amankulova, K., Szatmári, J., Urinov, J., Narmanov, Z., Nosirov, J. and Mucsi, L., 2023. Combining PlanetScope and Sentinel-2 images with environmental data for improved wheat yield estimation. International Journal of Digital Earth, 16(1), pp.847-867.
19. ESRI. 2023a. ArcGIS Pro: Release: 3.0.0. Redlands, CA: Environmental Systems Research Institute.
20. Richards, J.A., Jia, X., Richards, J.A. and Jia, X., 1999. Error correction and registration of image data. Remote Sensing Digital Image Analysis: An Introduction, pp.39-74.
21. ESRI. 2023b. ArcGIS Field Maps: Release: 23.1.1. Redlands, CA: Environmental Systems Research Institute.
22. Berhane, T.M., Costa, H., Lane, C.R., Anenkhonov, O.A., Chepinoga, V.V. and Autrey, B.C., 2019. The influence of region of interest heterogeneity on classification accuracy in wetland systems. Remote sensing, 11(5), p.551.
23. Cao, J., Leng, W., Liu, K., Liu, L., He, Z. and Zhu, Y., 2018. Object-based mangrove species classification using unmanned aerial vehicle hyperspectral images and digital surface models. Remote Sensing, 10(1), p.89.
24. Yeom, J., Jung, J., Chang, A., Ashapure, A., Maeda, M., Maeda, A. and Landivar, J., 2019. Comparison of vegetation indices derived from UAV data for differentiation of tillage effects in agriculture. Remote Sensing, 11(13), p.1548.
25. Song, B. and Park, K., 2020. Detection of aquatic plants using multispectral UAV imagery and vegetation index. Remote Sensing, 12(3), p.387.
26. Tucker, C.J., 1979. Red and photographic infrared linear combinations for monitoring vegetation. Remote sensing of Environment, 8(2), pp.127-150.
27. Bendig, J., Yu, K., Aasen, H., Bolten, A., Bennertz, S., Broscheit, J., Gnyp, M.L. and Bareth, G., 2015. Combining UAV-based plant height from crop surface models, visible, and near infrared vegetation indices

for biomass monitoring in barley. International Journal of Applied Earth Observation and Geoinformation, 39, pp.79-87.

28. Barnes, E.M., Clarke, T.R., Richards, S.E., Colaizzi, P.D., Haberland, J., Kostrzewski, M., Waller, P., Choi, C., Riley, E., Thompson, T. and Lascano, R.J., 2000. Coincident detection of crop water stress, nitrogen status and canopy density using ground based multispectral data. In Proceedings of the fifth international conference on precision agriculture, Bloomington, MN, USA (Vol. 1619, p. 6).
29. Rouse, J.W., Haas, R.H., Schell, J.A. and Deering, D.W., 1974. Monitoring vegetation systems in the Great Plains with ERTS. NASA Spec. Publ, 351(1), p.309.
30. Peñuelas, J., Gamon, J.A., Fredeen, A.L., Merino, J. and Field, C.B., 1994. Reflectance indices associated with physiological changes in nitrogen-and water-limited sunflower leaves. Remote sensing of Environment, 48(2), pp.135-146.
31. Feng, Q., Liu, J. and Gong, J., 2015. UAV remote sensing for urban vegetation mapping using random forest and texture analysis. Remote sensing, 7(1), pp.1074-1094.
32. Cheng, Y., Vrieling, A., Fava, F., Meroni, M., Marshall, M. and Gachoki, S., 2020. Phenology of short vegetation cycles in a Kenyan rangeland from PlanetScope and Sentinel-2. Remote sensing of environment, 248, p.112004.
33. Haralick, R.M., Shanmugam, K. and Dinstein, I.H., 1973. Textural features for image classification. IEEE Transactions on systems, man, and cybernetics, (6), pp.610-621.
34. Mohammadpour, P., Viegas, D.X. and Viegas, C., 2022. Vegetation mapping with random forest using sentinel 2 and GLCM texture feature—a case study for Lousã region, Portugal. Remote Sensing, 14(18), p.4585.
35. Zvoleff, A., 2020. glcm: Calculate Textures from Grey-Level Co-Occurrence Matrices R package version 1.6.5. Available from: https://CRAN.R-project.org/package=glcm
36. R Core Team. 2023. R: A Language and Environment for Statistical Computing Vienna, Austria: R Foundation for Statistical Computing. Retrieved from https://www.r-project.org/.
37. Anys, H., A. Bannari, D. C. He, and D. Morin. 1994. "Texture analysis for the mapping of urban areas using airborne MEIS-II images." Proceedings of the First International Airborne Remote Sensing Conference and Exhibition 3: 231-245.
38. Matese, A., Di Gennaro, S.F. and Berton, A., 2017. Assessment of a canopy height model (CHM) in a vineyard using UAV-based multispectral imaging. International Journal of Remote Sensing, 38(8-10), pp.2150-2160.
39. Wold S, Sjöström M, Eriksson L. 2001. PLS-regression: a basic tool of chemometrics. Chemometrics and Intelligent Laboratory Systems; 58(2):109-130.
40. Liland, K.H., Mevik, B.H., Wehrens, R. and Hiemstra, P., 2023. pls: Partial least squares and principal component regression. R package version 2.8-2, Available from: https://CRAN.R-project.org/package=pls
41. Cleve, C., Kelly, M., Kearns, F.R. and Moritz, M., 2008. Classification of the wildland–urban interface: A comparison of pixel-and object-based classifications using high-resolution aerial photography. Computers, Environment and Urban Systems, 32(4), pp.317-326.
42. Yu, Q., Gong, P., Clinton, N., Biging, G., Kelly, M. and Schirokauer, D., 2006. Object-based detailed vegetation classification with airborne high spatial resolution remote sensing imagery. Photogrammetric Engineering & Remote Sensing, 72(7), pp.799-811.
43. Li, X. and Shao, G., 2013. Object-based urban vegetation mapping with high-resolution aerial photography as a single data source. International journal of remote sensing, 34(3), pp.771-789.
44. Breiman, L., 2001. Random forests. Machine learning, 45, pp.5-32.
45. De Castro, A.I., Torres-Sánchez, J., Peña, J.M., Jiménez-Brenes, F.M., Csillik, O. and López-Granados, F., 2018. An automatic random forest-OBIA algorithm for early weed mapping between and within crop rows using UAV imagery. Remote Sensing, 10(2), p.285.
46. Ramos, A.P.M., Osco, L.P., Furuya, D.E.G., Gonçalves, W.N., Santana, D.C., Teodoro, L.P.R., da Silva Junior, C.A., Capristo-Silva, G.F., Li, J., Baio, F.H.R. and Junior, J.M., 2020. A random forest ranking approach to predict yield in maize with uav-based vegetation spectral indices. Computers and Electronics in Agriculture, 178, p.105791.
47. Puissant, A., Rougier, S. and Stumpf, A., 2014. Object-oriented mapping of urban trees using Random Forest classifiers. International Journal of Applied Earth Observation and Geoinformation, 26, pp.235-245.
48. Mather, P.M. and Koch, M., 2011. Computer processing of remotely-sensed images: an introduction. John Wiley & Sons.
49. Congalton, R.G. and Green, K., 2019. Assessing the accuracy of remotely sensed data: principles and practices. CRC press.
50. Cooper, S., Okujeni, A., Jänicke, C., Clark, M., van der Linden, S. and Hostert, P., 2020. Disentangling fractional vegetation cover: Regression-based unmixing of simulated spaceborne imaging spectroscopy data. Remote Sensing of Environment, 246, p.111856.

51. Fotheringham, A.S., Brunsdon, C. and Charlton, M., 2003. Geographically weighted regression: the analysis of spatially varying relationships. John Wiley & Sons.
52. Akaike, H., 1974. A new look at the statistical model identification. IEEE transactions on automatic control, 19(6), pp.716-723.
53. Furby, S., Zhu, M., Wu, X. and Wallace, J.F., 2008. Vegetation Trends 1990-2008, South Wester Agricultural Region of Western Australia, 2008 Update of the Land Monitor II Project. Product # 3 – Vegetation Trends, CSIRO Mathematical and Information Sciences.
54. Draper, N.R. and Smith, H., 1998. Applied regression analysis (Vol. 326). John Wiley & Sons.
55. Robinson, T.P., Novelly, P.E., Corner, R., Thomas, P., Russell-Brown, A., 2012. Pastoral Lease Assessment using Geospatial Analysis, Resource Management Technical Report 385, Department of Agriculture and Food, 74 pp.
56. Landis, J.R. and Koch, G.G., 1977. The measurement of observer agreement for categorical data. biometrics, pp.159-174.
57. Miles, J., 2005. R-squared, adjusted R-squared. Encyclopedia of statistics in behavioural science.
58. McQuarrie, A.D. and Tsai, C.L., 1998. Regression and time series model selection. World Scientific.
59. Wilson, L., van Dongen, R., Cowen, S. and Robinson, T.P., 2022. Mapping restoration activities on Dirk Hartog Island using remotely piloted aircraft imagery. Remote Sensing, 14(6), p.1402.
60. Bolyn, C., Michez, A., Gaucher, P., Lejeune, P. and Bonnet, S., 2018. Forest mapping and species composition using supervised per pixel classification of Sentinel-2 imagery. Biotechnologie, Agronomie, Société et Environment, 22(3).
61. Hemmerling, J., Pflugmacher, D. and Hostert, P., 2021. Mapping temperate forest tree species using dense Sentinel-2 time series. Remote Sensing of Environment, 267, p.112743.
62. Pu, R.L.; Cheng, J. 2015. Mapping forest leaf area index using reflectance and textural information derived from worldview-2 imagery in a mixed natural forest area in Florida, US., International Journal of Applied Earth Observation and Geoinformation. 42, 11–23.
63. Darvishzadeh, R.; Atzberger, C.; Skidmore, A.K.; Abkar, A.A. 2009 Leaf area index derivation from hyperspectral vegetation indicesand the red edge position. International Journal of Remote Sensing, 30, 6199–6218.
64. Robinson, T.P. et al. (2016) 'Testing the discrimination and detection limits of worldview-2 imagery on a challenging invasive plant target', International Journal of Applied Earth Observation and Geoinformation, 44, pp. 23–30.
65. Oumar, Z., Mutanga, O., 2014. Integrating environmental variables andWorldView-2 image data to improve the prediction and mapping of Thaumastocoris peregrinus (bronze bug) damage in plantation forests. ISPRS Journal of Photogrammetry and Remote Sensing. 87, 39–46.
66. Zhu, Yuanhui, Kai Liu, Lin Liu, Soe W. Myint, Shugong Wang, Hongxing Liu, and Zhi He. 2017. "Exploring the Potential of WorldView-2 Red-Edge Band-Based Vegetation Indices for Estimation of Mangrove Leaf Area Index with Machine Learning Algorithms" Remote Sensing 9, no. 10: 1060.
67. Mohan, M., Silva, C.A., Klauberg, C., Jat, P., Catts, G., Cardil, A., Hudak, A.T. and Dia, M., 2017. Individual tree detection from unmanned aerial vehicle (UAV) derived canopy height model in an open canopy mixed conifer forest. Forests, 8(9), p.340.
68. Jin, Y., Liu, X., Chen, Y. and Liang, X., 2018. Land-cover mapping using Random Forest classification and incorporating NDVI time-series and texture: A case study of central Shandong. International journal of remote sensing, 39(23), pp.8703-8723.
69. Zheng, H., Du, P., Chen, J., Xia, J., Li, E., Xu, Z., Li, X. and Yokoya, N., 2017. Performance evaluation of downscaling Sentinel-2 imagery for land use and land cover classification by spectral-spatial features. Remote Sensing, 9(12), p.1274.
70. Immitzer, M.; Atzberger, C.; Koukal, T. Tree Species Classification with Random Forest Using Very High Spatial Resolution 8-Band WorldView-2 Satellite Data. Remote Sens. 2012, 4, 2661-2693. https://doi.org/10.3390/rs4092661
71. Paczkowska, G. 1995a. Allocasuarina lehmanniana (Miq.) L.A.S.Johnson Available online: https://florabase.dbca.wa.gov.au/browse/profile/1733 (accessed on 20/11/2023).
72. Paczkowska, G. 1996a. Scaevola crassifolia Labill. Available online: https://florabase.dbca.wa.gov.au/browse/profile/7606 (accessed on 20/11/2023).
73. Paczkowska, G. 1996b. Melaleuca cardiophylla F.Muell. Available online: https://florabase.dbca.wa.gov.au/browse/profile/5887 (accessed on 20/11/2023).
74. Spooner, A. 1997a. Myoporum insulare R.Br. Available online: https://florabase.dbca.wa.gov.au/browse/profile/7291 (accessed on 20/11/2023).
75. Paczkowska, G. 1995b. Calothamnus quadrifidus R.Br. Available online: https://florabase.dbca.wa.gov.au/browse/profile/5426 (accessed on 20/11/2023).
76. Paczkowska, G. 1996c. Spyridium globulosum (Labill.) Benth. Available online: https://florabase.dbca.wa.gov.au/browse/profile/4828 (accessed on 20/11/2023).

77. Spooner, A. 1999. Grevillea preissii Meisn. Available online: https://florabase.dbca.wa.gov.au/browse/profile/8839 (accessed on 20/11/2023).
78. Spooner, A. 2005. Templetonia retusa (Vent.) R.Br. Available online: https://florabase.dbca.wa.gov.au/browse/profile/4256 (accessed on 20/11/2023).
79. Paczkowska, G. 1996d. Gomphocarpus fruticosus (L.) W.T.Aiton Available online: https://florabase.dbca.wa.gov.au/browse/profile/6587 (accessed on 20/11/2023).
80. Paczkowska, G. 1993a. Avena barbata Link Available online: https://florabase.dbca.wa.gov.au/browse/profile/233 (accessed on 20/11/2023).
81. Paczkowska, G. 1993b. Lagurus ovatus L. Available online: https://florabase.dbca.wa.gov.au/browse/profile/467 (accessed on 20/11/2023).
82. Spooner, A. 1997b. Austrostipa elegantissima (Labill.) S.W.L.Jacobs & J.Everett Available online: https://florabase.dbca.wa.gov.au/browse/profile/17237 (accessed on 20/11/2023).
83. Prošek, J. and Šímová, P., 2019. UAV for mapping shrubland vegetation: Does fusion of spectral and vertical information derived from a single sensor increase the classification accuracy?. International Journal of Applied Earth Observation and Geoinformation, 75, pp.151-162.
84. Lu, B. and He, Y., 2018. Optimal spatial resolution of Unmanned Aerial Vehicle (UAV)-acquired imagery for species classification in a heterogeneous grassland ecosystem. GIScience & Remote Sensing, 55(2), pp.205-220.
85. Rupasinghe, P.A., Simic Milas, A., Arend, K., Simonson, M.A., Mayer, C. and Mackey, S., 2019. Classification of shoreline vegetation in the Western Basin of Lake Erie using airborne hyperspectral imager HSI2, Pleiades and UAV data. International Journal of Remote Sensing, 40(8), pp.3008-3028.
86. Wang, H., Han, D., Mu, Y., Jiang, L., Yao, X., Bai, Y., Lu, Q. and Wang, F., 2019. Landscape-level vegetation classification and fractional woody and herbaceous vegetation cover estimation over the dryland ecosystems by unmanned aerial vehicle platform. Agricultural and Forest Meteorology, 278, p.107665.
87. Che'Ya, N.N., Dunwoody, E. and Gupta, M., 2021. Assessment of weed classification using hyperspectral reflectance and optimal multispectral UAV imagery. Agronomy, 11(7), p.1435.
88. Sothe, C., Dalponte, M., Almeida, C.M.D., Schimalski, M.B., Lima, C.L., Liesenberg, V., Miyoshi, G.T. and Tommaselli, A.M.G., 2019. Tree species classification in a highly diverse subtropical forest integrating UAV-based photogrammetric point cloud and hyperspectral data. Remote Sensing, 11(11), p.1338.
89. Adão, T., Hruška, J., Pádua, L., Bessa, J., Peres, E., Morais, R. and Sousa, J.J., 2017. Hyperspectral imaging: A review on UAV-based sensors, data processing and applications for agriculture and forestry. Remote sensing, 9(11), p.1110.
90. Blaschke, T., Lang, S., Lorup, E., Strobl, J. and Zeil, P., 2000. Object-oriented image processing in an integrated GIS/remote sensing environment and perspectives for environmental applications. Environmental information for planning, politics and the public, 2(1995), pp.555-570.
91. Whiteside, T.G., Boggs, G.S. and Maier, S.W., 2011. Comparing object-based and pixel-based classifications for mapping savannas. International Journal of Applied Earth Observation and Geoinformation, 13(6), pp.884-893.
92. Sreenivasulu, P. and Chaitanya, N.K., 2014. Removal of Salt and Pepper Noise for Various Images Using Median Filters: A Comparative Study. IUP Journal of Telecommunications, 6(2).
93. Lu, D., Hetrick, S. and Moran, E., 2011. Impervious surface mapping with Quickbird imagery. International journal of remote sensing, 32(9), pp.2519-2533.
94. Pérez-Ortiz, M., Peña, J.M., Gutiérrez, P.A., Torres-Sánchez, J., Hervás-Martínez, C. and López-Granados, F., 2016. Selecting patterns and features for between-and within-crop-row weed mapping using UAV-imagery. Expert Systems with Applications, 47, pp.85-94.
95. Ma, L., Cheng, L., Li, M., Liu, Y. and Ma, X., 2015. Training set size, scale, and features in Geographic Object-Based Image Analysis of very high resolution unmanned aerial vehicle imagery. ISPRS Journal of Photogrammetry and Remote Sensing, 102, pp.14-27.
96. Li M. 2003. The method of vegetation fraction estimation by remote sensing. Beijing: Chinese Academy of Sciences
97. Escribano, P. et al. 2010. Spectral properties and sources of variability of ecosystem components in a Mediterranean semiarid environment, Journal of Arid Environments, 74(9), pp. 1041–1051.
98. Propastin, P.A., 2009. Spatial non-stationarity and scale-dependency of prediction accuracy in the remote estimation of LAI over a tropical rainforest in Sulawesi, Indonesia. Remote Sensing of Environment, 113(10), pp.2234-2242.
99. Hu, Q., Ma, Y., Xu, B., Song, Q., Tang, H. and Wu, W., 2018. Estimating sub-pixel soybean fraction from time-series MODIS data using an optimized geographically weighted regression model. Remote Sensing, 10(4), p.491.

 doi:10.20944/preprints202312.0441.v1

disclaim responsibility for any injury to people or property resulting from any ideas, methods, instructions or products referred to in the content.